Reduced fluids in porphyry copper-gold systems reflect the occurrence of the wall-rock thermogenic process: An example from the No.1 deposit in the Xiongcun district, Tibet, China

Xinghai Lang[a,b,*], Yulin Deng[a,*], Xuhui Wang[a], Juxing Tang[c], Fuwei Xie[a], Zongyao Yang[d], Qing Yin[a], Kai Jiang[e]

[a] College of Earth Science and MNR Key Laboratory of Tectonic Controls on Mineralization and Hydrocarbon Accumulation, Chengdu University of Technology, Chengdu 610059, China
[b] State Key Laboratory of Ore Deposit Geochemistry, Institute of Geochemistry, Chinese Academy of Sciences, Guiyang 550002, China
[c] Institute of Mineral Resources, Chinese Academy of Geological Sciences, Beijing 100037, China
[d] Faculty of Geosciences and Environmental Engineering, Southwest Jiaotong University, Chengdu 611756, China
[e] Tibet Tianyuan Mineral Exploration Co. Ltd., Xigaze 857000, China

ABSTRACT

High fO_2 conditions characterize the majority of global porphyry copper deposits and contain highly oxidized minerals, such as magnetite and anhydrite. In contrast, the No. 1 porphyry Cu–Au deposit in the Xiongcun district (Tibet, China) has abundant pyrrhotite, reduced fluids ($CH_4 \gg CO_2$), and a relative lack of highly oxidized minerals, which are indicative of low fO_2 conditions. Scanning electron microscopy, fluid inclusion, C–H–O–He–Ar isotopes, and whole-rock organic carbon contents and isotope analysis were used to constrain the evolution of ore-forming fluid, the origin of CH_4 and metal deposition mechanisms for the No. 1 deposit. The He–Ar isotopic compositions ($^3He/^4He = 0.11–0.96$ Ra, $^{40}Ar/^{36}Ar = 418.7–2920.2$) suggest that the ore-forming fluids predominantly derived from crust source with minor mantle input. The H–O isotopic analysis results ($\delta^{18}O_{H2O} = -1.8$ to $+5.2‰$, $\delta D = -106$ to $-89.9‰$) indicate that the ore-forming fluids were derived from a magmatic source that mixed with some meteoric waters. The element compositions of zircons and fluid/melt inclusions from the mineralized Middle Jurassic quartz diorite porphyry reveal that the primary magma was characterized by high log fO_2 ($>$ NNO) conditions. The quartz diorite porphyry intruded into the carbon-bearing wall rocks produced abundant CH_4 by thermal decomposition of organic matter ($\delta^{13}C_{CH4} = -26.3$ to $-28.5‰$), which changed the redox state of the porphyry copper system from oxidized to reduced condition. Ore elements were deposited via fluid boiling as a consequence of the rapid decrease in temperature and pressure.

1. Introduction

The majority of global porphyry Cu deposits are a result of subduction-related or post-collision magmatism that generates highly oxidized magmas (i.e., $\log fO_2 >$ FMQ + 2, Mungall, 2002; Richards, 2003) and hydrothermal fluids with CO_2, which crystalize highly oxidized minerals (e.g., magnetite, anhydrite) (Sillitoe, 2010). Examples of these such deposits include the Bingham Cu–Mo deposit in the U.S.A (Roedder, 1971), the Elatsite Cu–Au deposit in Bulgaria (Stefanova et al., 2014), the Bajo de la Alumbrera Cu–Au deposit in Argentina (Ulrich, 2002), and the Qulong Cu–Mo deposit in China (Xiao et al., 2012). To some extent, such oxidized magmas can carry on massive metals, and control them effective deposition in appropriate location instead of premature occurring (Hedenquist and Lowenstern, 1994; Cooke et al., 2005; Richards, 2003, 2011). Nevertheless, a growing body of evidence suggests the existence of reduced porphyry copper deposits (Rowins, 1999, 2000). Generally, these porphyry deposits are formed by CH_4-rich hydrothermal fluids and contain abundant hypogene pyrrhotite but lack oxidized minerals. In recent years, reduced porphyry copper systems (e.g., the Catface, Smith et al., 2012; Baogutu Cu–Mo, Cao et al., 2014a; Pulang Cu deposits, Liu et al., 2013) were recognized to be related to oxidized magmas, consistent with classic oxidized porphyry copper deposits (e.g., the Bingham, Qulong Cu–Mo and Elatsite Cu–Au deposit), that became reduced during the evolution of the magmatic-hydrothermal system (Cao et al., 2014a,b, 2017; Shen and Pan, 2015). Although previous studies have revealed the geological

characteristics of these deposits, the evolution of ore-forming fluid, particularly the origin of CH_4 and metal deposition mechanisms at work are less clear.

The No. 1 deposit (also name Xiongcun deposit, e.g., Xu et al., 2009; Xietongmen deposit, e.g., Tafti et al., 2009) in the Xiongcun district, Tibet, is a subduction-related porphyry copper deposit in the Gangdese porphyry copper belt (GPCB) (Lang et al., 2014a; Tang et al., 2015). The No. 1 deposit contains CH_4-rich hydrothermal fluid and hypogene pyrrhotite, with a relative lack of highly oxidized magnetite–anhydrite assemblages (Tang et al., 2015), which can be classified as a reduced porphyry copper deposit referring to Rowins (2000). Hence, the No.1 deposit is an excellent field site to understand the evolution of ore-forming fluid, the origin of CH_4 and metal deposition mechanisms for reduced porphyry copper deposit.

Unfortunately, previous studies have mainly focused on the geological characteristics, geochronology, source of ore-forming metals and fluid, petrogenesis, tectonic setting of the No. 1 deposit (Xu et al., 2009; Tafti et al., 2014; Lang et al., 2014a; Tang et al., 2015; Wang et al., 2017). In this study, we use cathodoluminescence petrography, fluid inclusion microthermometry, Raman microspectroscopy, C–H–O–-He–Ar isotope, scanning electron microscopy-energy dispersive spectrometer, and whole-rock organic carbon contents and isotope analyses, to constrain the evolution of ore-forming fluid, origin of CH_4 and metal deposition mechanisms in the No. 1 deposit. This study will advance our understanding of reduced porphyry copper deposit genesis and metallogenesis in the GPCB.

2. Regional geological setting

The Tibetan plateau, bound by the Jinshajiang suture zone (JSSZ), Bangong–Nujiang suture zone (BNSZ), and Yarlung–Zangbo suture zone (YZSZ) from north to south, can be divided into the Qiangtang terrane, Lhasa terrane, and Himalayas (Fig. 1a, b, Yin and Harrison, 2000; Zhu et al., 2013), respectively. The Lhasa terrane, which can be divided into northern, central, and southern subterranes by the Shiquan River–Nam Tso Mélange Zone (SNMZ) and the Luobadui–Milashan Fault (LMF), is bounded to the north by the Banggong–Nujiang Suture Zone (BNSZ) and to the south by the Yarlung–Zangbo Suture Zone (YZSZ, Fig. 1b, c). The southern Lhasa subterrane contains Mesozoic and Cenozoic granitoids, as well as dispersed Mesozoic–Cenozoic volcanic–sedimentary rocks (Pan et al., 2006; Zhu et al., 2011). The Mesozoic and Cenozoic granitoids are mainly composed of Late Triassic to Cretaceous subduction-related arc granitoids and Paleocene–Miocene collision-related granitoids (Mo et al., 2003; Zhu et al., 2011; Wang et al., 2015). The Mesozoic–Cenozoic volcanic–sedimentary rock mainly consists of the Lower–Middle Jurassic Yeba and Xiongcun Formation, the Middle Triassic–Lower Cretaceous Sangri Group (Kang et al., 2014; Wang et al., 2016; Wei et al., 2017; Lang et al., 2019a,b), and the Paleocene–Eocene Linzizong volcanic succession (Mo et al., 2003; Lee et al., 2009).

The GPCB is 50 km wide and 400 km-long and situated at the southern margin of the Lhasa terrane (Hou et al., 2009; Zheng et al., 2014). Based on the magmatic and tectonic evolution associated with the ore deposit formation, previous studies have identified three main phases (Fig. 1c): (1) 180–160 Ma, the Xiongcun porphyry Cu–Au deposits (including No.1, No.2 and No.3 deposits) represent a mineralization event related to the subduction of the New-Tethys (Lang et al., 2014a, 2019c; Tang et al., 2015), (2) 65–40 Ma, the Sharang porphyry Mo, the Mengya'a skarn Pb–Zn, and the Sinongduo low-sulfidation epithermal Pb–Zn–Ag deposits formed during Indian–Asian collision that generated porphyry-skarn and epithermal deposits (Zhao et al., 2014; Tang et al., 2016; Fu et al., 2017), and (3) 20–10 Ma, the occurrence of Indian–Asian post-collision-related porphyry-skarn Cu–(Mo) deposits, including the Qulong, Jiama, Chongjiang, Tinggong, Zhunuo, and Jiru Cu–(Mo) deposits (Xie et al., 2006; Zheng et al., 2007, 2016; Zhang et al., 2008; Yang et al., 2009; Chen et al., 2014).

3. Deposit geology

The Xiongcun district is located in the middle region of the southern Lhasa terrane, 53 km west of Xigaze (Fig. 1c), which is composed of three individual deposits, the No. 1, No. 2, and No. 3 deposit (Fig. 1d). The Xiongcun district is structurally complex, containing Early Jurassic to Eocene rock units (Fig. 1d). The Xiongcun Formation is exposed throughout the Xiongcun district, which consists of conglomerate, sandstone, siltstone, carbonaceous shale/slate, argillite, volcanic breccia, lava, and subordinate limestone (195–165 Ma, Lang et al., 2019,b). Intrusive rocks include Early Jurassic quartz diorite porphyry (181–175 Ma, Lang et al., 2014a; Tafti et al., 2014), Early–Middle Jurassic quartz diorite porphyry (174 Ma, Lang et al., 2014b), Middle Jurassic quartz diorite (167–161 Ma, Lang et al., 2014a), diabase dykes (165 Ma, Lang et al., 2018), late Jurassic granodiorite porphyry, and Eocene biotite granodiorite, quartz diorite, granitic aplite dykes, and lamprophyre dykes (Lang et al., 2017, Fig. 1d, e). The F1 and F2 faults are the main structures in the Xiongcun district, and they occur along the hangingwall and footwall of the No. 1 deposit. Other post-mineralization faults are distributed in bands, which are mainly NE-, N-, EW-, and NW-trending. The southern margin of the Xiongcun district has a developed EW-trending anticline (Fig. 1d, e). Constrained via Re-Os isotopic dating of molybdenite, the Xiongcun district includes two individual mineralization events, which are represented by the No. 1 (161.5 ± 2.7 Ma) and No. 2 deposit (172.6 ± 2.1 Ma, Lang et al., 2014a) respectively. The No. 3 deposit is a newly discovered porphyry Cu–Au deposit similar to the No. 2 deposit (Lang et al., 2019c).

The No. 1 deposit is mainly hosted in the Middle Jurassic quartz diorite porphyry (167–161 Ma) and the surrounding Xiongcun Formation tuff (Fig. 1e, Tafti et al., 2014; Tang et al., 2015). The quartz diorite porphyry associated with mineralization is intensely altered, and protolith texture and composition are poorly recognized. The host intrusion contains round to square quartz eyes, which are up to 1.5 cm in diameter and account for 10 to > 15 vol%. The wall rocks adjacent to the intrusion are composed of fine- to medium-grained tuff. These wall rocks are usually highly affected by alteration. The shape of the No. 1 deposit is entirely ellipsoidal or fusiform; the ore body is 1300 m-long and up to 600 m-wide with an average thickness of approximately 250 m. The No. 1 deposit contains the following resources: 1.04 Mt of Cu, 143.31 t of Au, and 900.43 t of Ag, with average grades of 0.48% Cu, 0.66 g/t Au, and 4.19 g/t Ag, respectively (Tang et al., 2012).

Alterations in the No. 1 deposit include potassic, phyllic, and propylitic alteration. Potassic alteration is spatially associated with the highest grade Cu and Au mineralization, rather than occurring in the transitional and outlying zones (Fig. 2, Supplementary Fig. 1). The alteration phases consist of abundant biotite, andalusite, minor K-feldspar, and magnetite (Supplementary Figs. 2 and 3). This alteration occurs throughout the center of the deposit, and elevated amounts of chalcopyrite, pyrite, and pyrrhotite occur in this zone. In the phyllic alteration, quartz, sericite, and pyrite are the main alteration minerals associated with minor mineralization. This alteration event overprinted the potassic alteration and is widely distributed outside of the potassic alteration zone. Propylitic alteration consists epidote, chlorite, calcite, and typically less than 2% disseminated pyrite assemblage, however, it only distributes locally as controlled by the fault (Chen et al., 2008; Lang et al., 2011; Huang et al., 2012; Tafti et al., 2014). Based on field mapping, core logging, and petrographic observations, we have established two stages of mineralization: (1) the magmatic-hydrothermal transitional stage (which corresponds to the quartz eyes formation) and (2) the hydrothermal stage (which is divided into sub-stage I, sub-stage II, and sub-stage III; Table 1). The major mineralization event occurs in sub-stage I.

4. Sampling and analytical methods

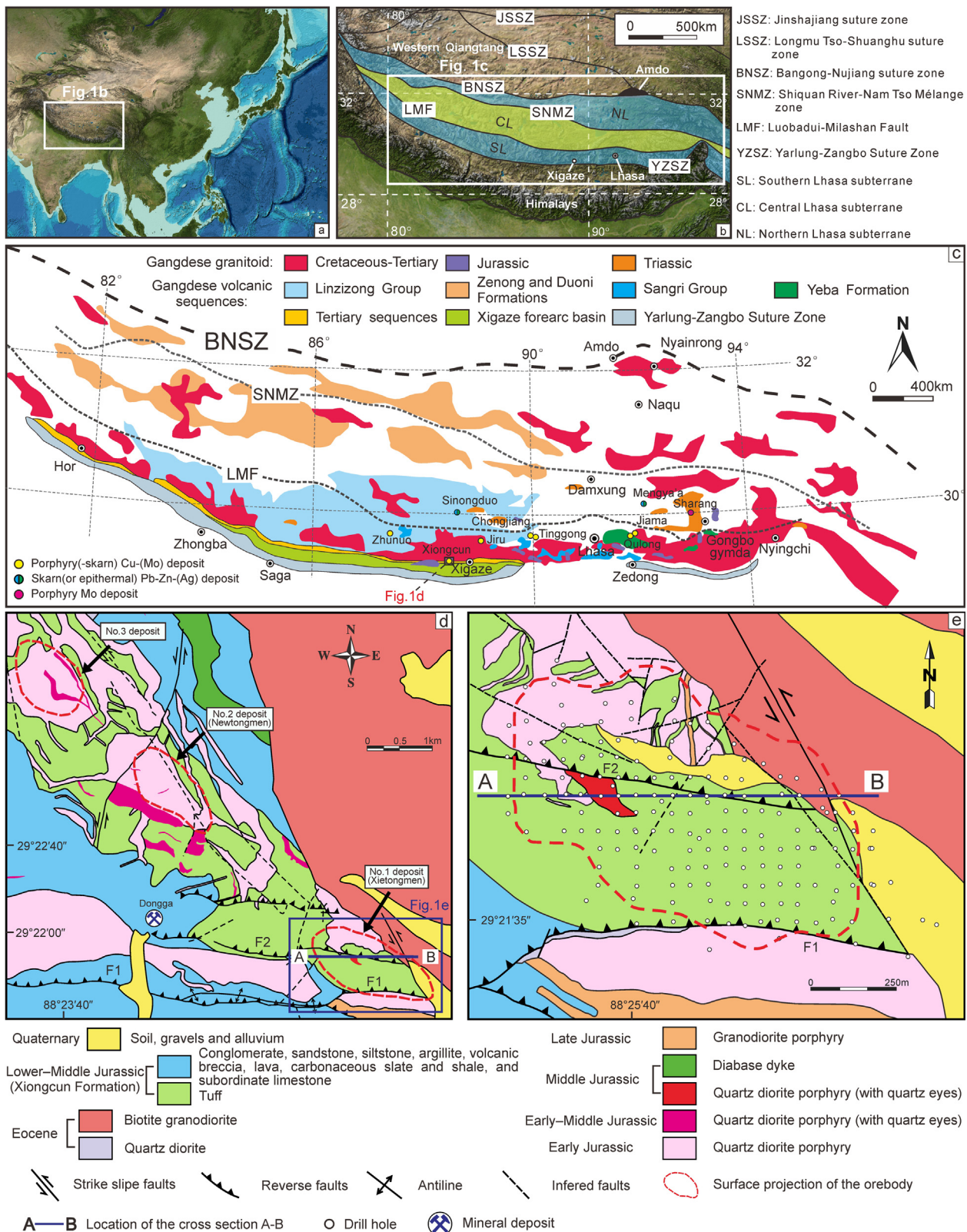Selected samples mainly originate from 14 diamond drill holes in

Fig. 1. (a) Simplified map showing the location of the Himalayan–Tibetan orogen. (b) Tectonic framework of the Lhasa terrane (modified after Zhu et al., 2011). (c) Diagram showing the distribution of magmatic rocks in the Lhasa terrane (modified after Wang et al., 2016). (d) Geologic map of the Xiongcun district (modified after Oliver, 2006). (e) Geologic map of the No.1 deposit (modified after Oliver, 2006).

the A–B cross section (Fig. 2). We analyzed over 60 samples for fluid inclusion studies. Sixteen of these samples were analyzed further by scanning electron microscopy-cathodoluminescence (SEM-CL),

microthermometry and Raman microspectroscopy. Nine quartz samples from the quartz veins were selected for C–H–O isotope analyses. Four sulfide and one quartz samples were chosen for He–Ar isotope analyses.
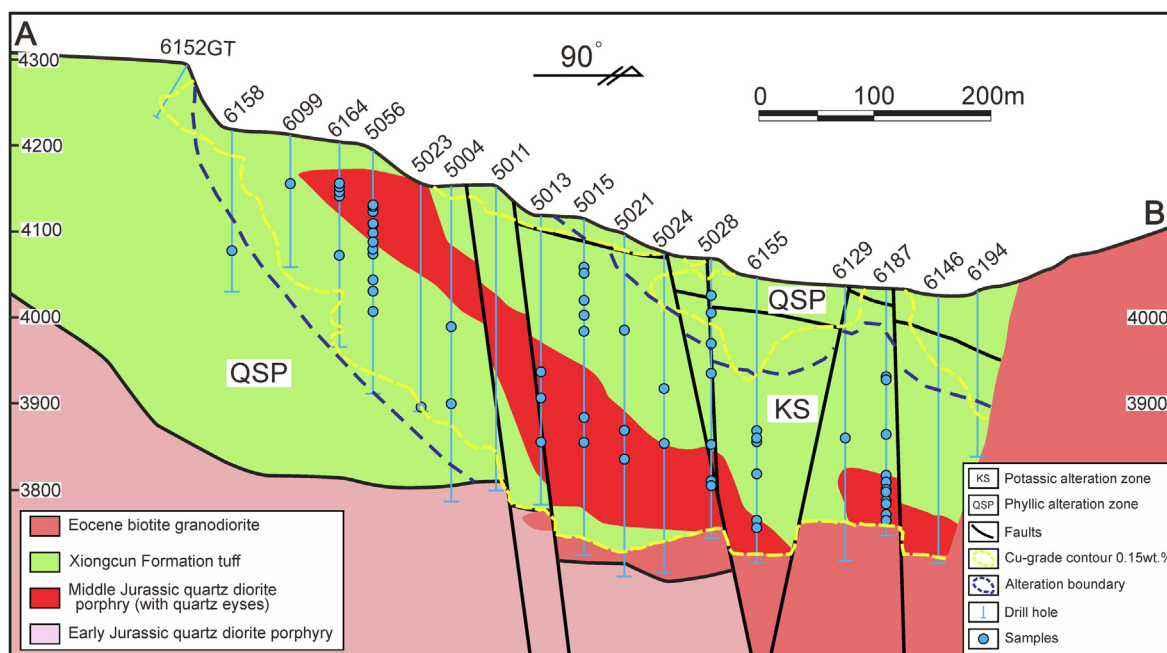
Fig. 2. Cross section of A–B (see Fig. 1d, e) of the No.1 deposit in the Xiongcun district showing the sample locations (modified after Tang et al., 2015).

Besides, five carbonaceous slate and shale samples from the Xiongcun Formation at outcrop were chosen for scanning electron microscopy-energy dispersive spectrometer (SEM-EDS) and whole-rock organic carbon contents and isotope analysis. The analytical methods and results are provided in the Supplementary material.

5. Results

5.1. Veins and quartz generations

We classified the mineralization-related veins in the No. 1 deposit based on the abundance of the vein-infill and alteration minerals. Crosscutting relationships in the drill-core samples were used to distinguish the relative timing of the different veins. We observed many types of veins in the No. 1 deposit (Table 1, Fig. 3), but several veins, especially sulfide-rich veins are inappropriate to fluid inclusion measurements and, therefore, are excluded from this study. According to SEM-CL imaging and petrographic observations, the quartz eyes and veins suitable for fluid inclusion studies are described below:

Quartz eyes: Quartz eyes in the ore-bearing quartz diorite porphyry are gray and rounded with a grain size that varies significantly from 2 to 15 mm (Fig. 3a, e, and f). Quartz eyes are mostly irregular with rounded outlines, although some small quartz eyes may have one or several short, straight edges. Some quartz eyes cross-cut by quartz veins (Fig. 3e). There are two petrographically distinct quartz eye types in the mineralized porphyry when observed under crossed polarized light and SEM-CL imaging: (1) Similar to typical quartz phenocrysts (e.g., Harris et al., 2004; Chang and Meinert, 2004), Type A consists of mono-crystalline quartz that has rounded and irregular anhedral crystals (Fig. 4a). However, quartz eyes can be cut by quartz veins or influenced by hydrothermal fluid in a later stage, which causes the formation of remnant quartz. The significant feature that identifies these occurrences is that the remnant quartz crystals have identical extinction angles under crossed polarized light. More commonly, quartz phenocrysts in porphyry stocks crystallized in a deep magma chamber and were then transported to their emplacement location (Vasyukova et al., 2013). These quartz eyes have no distinct oscillatory zoning or irregular resorption borders. Therefore, it is likely that adiabatic decompression, due to rapid magma ascent, influenced their magmatic-hydrothermal

transition; (2) Type B quartz eyes consists of sugary aggregates of anhedral quartz crystals (Fig. 4b). They are usually interpreted as miarolitic pods or cavities (e.g., Jahns and Burnham, 1969; Candela and Blevin, 1995; Harris et al., 2004), indicating that they were filled by quartz in a later hydrothermal stage.

Early quartz-sulfide veins (EQSV): EQSV are possibly the earliest generation of veins in the deposit. Any other vein types can cut them and have narrow alteration envelopes that contain biotite (Fig. 3b–d). These veins have irregular margins and a thickness of < 10 cm with no internal symmetry. A large number of sulfides, including chalcopyrite, pyrite and pyrrhotite occur in the veins. EQSV are hosted within and around the quartz diorite porphyry. We observe three generations of quartz using SEM-CL imaging (Fig. 4c): Q1 quartz is characterized by bright color and develops microfractures which were filled by later CL-gray quartz (Q2 and Q3). These textures are not observed using classical transmitted light microscopy.

Quartz-sulfide veins (QSV): Additionally, compared to the EQSV, the QSV have weak potassic alteration with distinct boundaries along the potassic alteration zones (Fig. 3e and f). Crosscutting relationships indicate that the QSV formed slightly later than the EQSV because they can cut biotite-sulfide veins (BSV). The vein walls are bent, and vein thickness ranges from < 10 to 20 cm. Sulfide minerals consist predominately of fine-grained pyrite, chalcopyrite and variable concentrations of pyrrhotite. QSV are dominated by quartz aggregates (Q4) and have consistently lower CL intensity than the Q1 quartz from the EQSV (Fig. 4d). In most QSV, late, dark irregular quartz patches (Q5) are widely distributed (Fig. 4d).

Late quartz veins (LQV): Late quartz veins can crosscut early quartz-sulfides veins. The veins vary from several millimeters to several centimeters in width and have straight contacts. Specific identification features for these veins include no mineralization, milky-white color, and nets contacts (Fig. 3g, l). The veins are dominated by CL-dark quartz (Q6), and quartz that occurs in clumps rather than equigranular aggregates (Fig. 4e).

Calcite veins (CV): CV are the youngest generation of veins observed and crosscut all other vein types. CV range in thickness from less than 2 mm to several centimeters have a pale yellow-white color, and typically have wavy vein walls (Fig. 3g, h, k).

Table 1
Major characteristics of hydrothermal stage from the No.1 deposit in the Xiongcun district

Stage	Vein type	Alteration type	Mineralization type	Vein distribution	Vein thickness	Fluid inclusion study
Sub-stage I	Early Quartz–sulfide veins (EQSV)	Potassic (Bt + As + Qtz + Kfs + Mus + Mag)	Py-Cpy ± Po	Porphyry	<10 cm	Used
	Biotite- sulfide veins (BSV)		Py-Cpy-Po	Porphyry, tuff	<0.3 cm	Not used
	Magnetite-sulfide veins (MSV)		Mag-Py-Cpy	Porphyry	<0.3 cm, up to 2 cm	Not used
	Quartz-molybdenite-sulfide veins (QMV)		Mo ± Py ± Cpy	Porphyry, tuff	<0.1 cm, up to 1 cm	Not used
	Quartz-sulfide veins (QSV)		Py-Cpy ± Po	Porphyry, tuff	<10 cm, up to 20 cm	Used
Sub-stage II	Pyrite veins (PV)	Phyllic (Qtz + Py + Ser)	Py ± Cpy ± Po	Porphyry, tuff	<2 cm, up to 5 cm	Not used
	Chalcopyrite-pyrite-pyrrhotite veins (CPPV)		Cpy-Py-Po	tuff	<5 cm, up to 100 cm	Not used
	Polymetallic veins (PMV)		Py-Cpy-Sp (± Po ± Cpy ± Gn)	tuff	<10 cm, up to 2 cm	Not used
Sub-stage III	Epidote veins (EV)	Propylitic (Ep + Chl + Cal)	No sulfides	Not widely developed	<1 cm,	Not used
	Late quartz veins (LQV)		Minor pyrite or none	Not widely developed	<3 cm, up to 10 cm	Used
	Calcite veins (CV)		No sulfides	Not widely developed	<0.5 cm	Used

Chl = chlorite, Sph = sphalerite, Ep = epidote, Qtz = quartz, Bt = biotite, Mag = magnetite, Kfs = K-feldspar, Mus = muscovite, As = andalusite, Cal = calcite, Cpy = chalcopyrite, Po = pyrrhotite, Gn = galena, Mo = molybdenite.

5.2. Fluid and melt inclusion types

In this study, we identified six fluid inclusion types (sub-classes) and two melt inclusion types (sub-classes) based on petrographic criteria at room temperature (Fig. 5; Supplementary Table 1). Fluid inclusion can be classified L (liquid-dominant), V (vapor-dominant) and H (halite-bearing), and then specified the sub-classes L1 (liquid-rich two-phase), L2 (liquid-vapor two-phase), V1 (vapor-rich two-phase), V2 (single-phase vapor), H1 (contains single halite daughter mineral), H2 (contains multiple daughter minerals – halite, sylvite, anhydrite and opaques) – based on relative proportions of different phases stable at room temperature. Furthermore, we identified M type inclusions in the quartz eyes (Type A), including M1 (melt only) and M2 (fluid-melt) sub-classes. The characteristics of fluid and melt inclusions are described as follows:

(1) L-type fluid inclusions are biphase liquid-rich inclusions with variable vapor proportions between 5 and 40 vol%. According to the average volume percent of bubble size, they can be further divided into L1 and L2. L1 type inclusions have relatively small vapor bubbles approximately occupied 5 to 15 vol%, whereas the vapor bubble proportions in L2 are 15 to 40 vol%. They occur as negative crystal shapes, with rounded or irregular morphologies and generally vary in size from 2 to 30 μm.

(2) V-type fluid inclusions are biphase inclusions with high vapor proportions, which are subdivided into V1 (> 60 vol% vapor) and V2 inclusions (single-phase vapor) based on the relative proportion of the vapor phase infill. They are ellipsoidal, elongated, negative crystal shaped or with irregular shapes, varying in size from 3 to 15 μm.

(3) H-type fluid inclusions contain daughter minerals and are rich in liquid with 5 to 20 vol% vapor. They generally have negative crystal shapes and have a typical size ranging between 4 and 10 μm. The H1-type fluid inclusions contain a single cubic-shape halite daughter mineral. The H2-type fluid inclusions contain multiple daughter crystals - halite and sylvite, ± other daughter minerals (e.g., anhydrite and/or opaque/unidentified minerals).

(4) Melt only (M1) and fluid-melt (M2) inclusions can also be observed in the quartz eyes (type A). M1-type fluid inclusions have melt ± metallic minerals ± vapor bubbles; however, compared to M1, M2-type inclusions have minor liquid infill. They all have sub-rounded or irregular shapes and generally vary in size from 10 to 30 μm. The melt inclusions can be subdivided into crystallized and glassy. Crystallized melt inclusions have an irregular shape and sparkly appearance, with a dark bubble at the crystal's edge (Fig. 5a). Glassy melt inclusions have relatively sharp borders and bright color when observed under the microscope (Fig. 5b–c).

5.3. Fluid inclusion microthermometry

Representative quartz and calcite samples from the quartz eyes (Type A), EQSV, QSV, LQV, and CV were chosen for the microthermometry experiments. We performed the microthermometric fluid inclusion measurements on primary fluid inclusion assemblages (FIAs) (Goldstein and Reynolds, 1994). All microthermometric data are listed in Supplementary Table 2.

Quartz eyes (Type A): We observed the M1, M2, L1, L2, H1, H2, V1 and V2 type fluid inclusions in quartz. Over 50% of the fluid inclusions are of V1, V2, and H2 types (Fig. 5; Supplementary Table 1). All of the hyper-saline fluid inclusions are homogenized by halite and sylvite dissolution. Halite dissolution temperatures for the H1-type range from 271 to 341 °C. These dissolution temperatures correspond to salinity of 35.9 to 41.6 wt% NaCl equiv. Halite and sylvite dissolution temperatures for the H2 inclusions range from 376 to 440 °C and 176 to 224 °C, respectively. These dissolution temperatures correspond to salinity of 57.9 to 62.8 wt% NaCl equiv for halite + sylvite-bearing inclusions
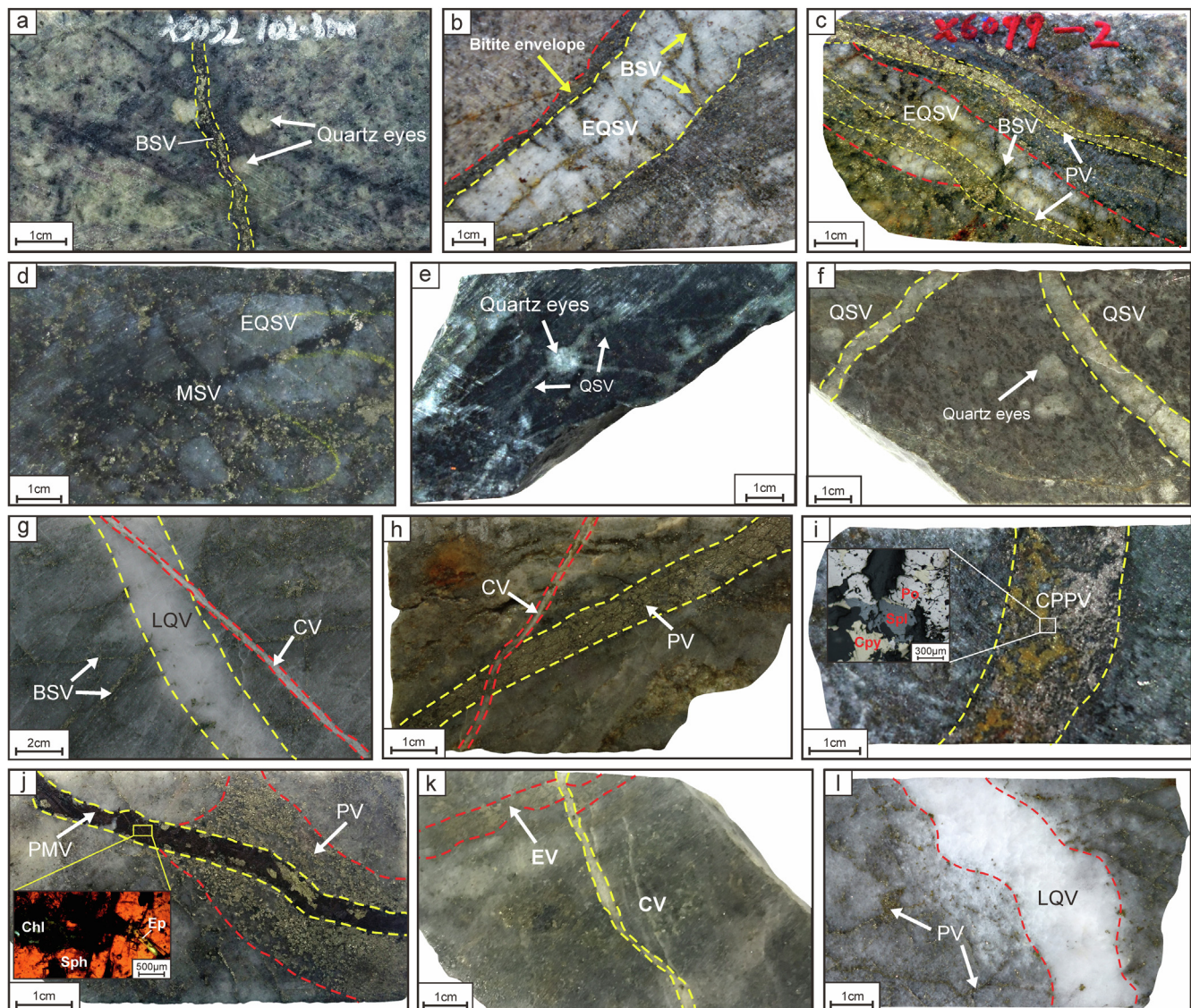
Fig. 3. Photographs of different vein types from the No.1 deposit in the Xiongcun district. (a) Biotite-sulfide veins and quartz eyes in potassic alteration zone; (b–d) Early quartz-sulfide veins cross-cut by biotite-sulfide vein, pyrite vein and magnetite-sulfide vein; (e–f) typical quartz-sulfide veins with weak potassic alteration, and some of them can cut quartz eyes; (g) Late quartz vein cut biotite-sulfide vein, and it cut by calcite vein; (h) Calcite vein cutting pyrite vein; (i) Typical chalcopyrite-pyrite-pyrrhotite vein; (j) Polymetallic vein cutting a pyrite vein; (k) Calcite vein cutting an epidote vein; (l) Pyrite veins cut by late quartz veins. EQSV = early quartz-sulfide veins, BSV = biotite sulfide veins, MSV = magnetite-sulfide veins, QSV = quartz-sulfide veins, PV = pyrite veins, PMV = polymetallic veins, EV = epidote veins, LQV = late quartz veins, CV = calcite veins, Chl = chlorite, Sph = sphalerite, Ep = epidote, Cpy = chalcopyrite, Po = pyrrhotite.

(Hall et al., 1988). V1 fluid inclusions homogenize to vapor phase between 421 and 471 °C and have Tm_{ice} of −3.5 to −5.7 °C, corresponding to low salinities that range from 5.7 to 8.8 wt% NaCl equiv.

EQSV: Fluid inclusion assemblages in the EQSV mainly consist of H2, L2, V1, and V2 types (Fig. 5; Supplementary Table 1); however, halite and sylvite are the only daughter minerals in the H2 type fluid inclusions. Homogenization by halite and sylvite dissolution after bubble disappearance was observed in all H1, H2 type inclusions. Final halite dissolution temperatures for the H1 type fluid inclusions range from 274 to 315 °C, and the corresponding salinities range between 36.3 and 39.3 wt% NaCl equiv. Halite and sylvite dissolution temperatures for the H2 type inclusions are 342 to 348 °C and 217 to 259 °C, respectively, corresponding to salinities 56.1 to 58.4 wt% NaCl equiv. The homogenization temperatures of V1-type fluid inclusions range from 396° to 422 °C, and the Tm_{ice} from −1.9 to −2.1 °C, corresponding to salinities 3.2 to 3.6 wt% NaCl equiv.

QSV: H1, L1 and L2, are the main fluid inclusion types in the QSV, which account for more than 80% of the veins (Fig. 5; Supplementary Table 1). The majority of the hyper-saline fluid inclusions (H1) are homogenized by halite dissolution rather than vapor bubble disappearance. Tm(halite) range from 153 to 260 °C, corresponding to the salinity of 29.8 to 35.3 wt% NaCl equiv; homogenization temperatures range from 157 to 211 °C. The L2-type fluid inclusion homogenization temperatures vary from 227 to 261 °C, and Tm_{ice} from −14.8 to −17.3 °C, corresponding to a wide range of salinities between 18.2 and 20.5 wt% NaCl equiv. L1-type fluid inclusions homogenize at temperatures between 159 and 228 °C, show Tm_{ice} from −5.0 to −19.0 °C, corresponding to salinities from 7.9 to 21.7 wt% NaCl equiv.

LQV and CV: L1-type fluid inclusions are common in the LQV and CV (Fig. 5; Supplementary Table 1). Their homogenization temperatures in the LQV range from 150 to 186 °C, Tm_{ice} from −0.5 to −6.3 °C, and the corresponding salinity from 0.9 to 9.6 wt% NaCl equiv. L1-type fluid inclusions in the CV veins show relatively low Tm_{ice} (−0.5 to −2.4 °C), salinities between 0.9 and 4.0 wt% NaCl equiv, and low homogenization temperatures (132–141 °C) compared with the same fluid inclusion type in the LQV.
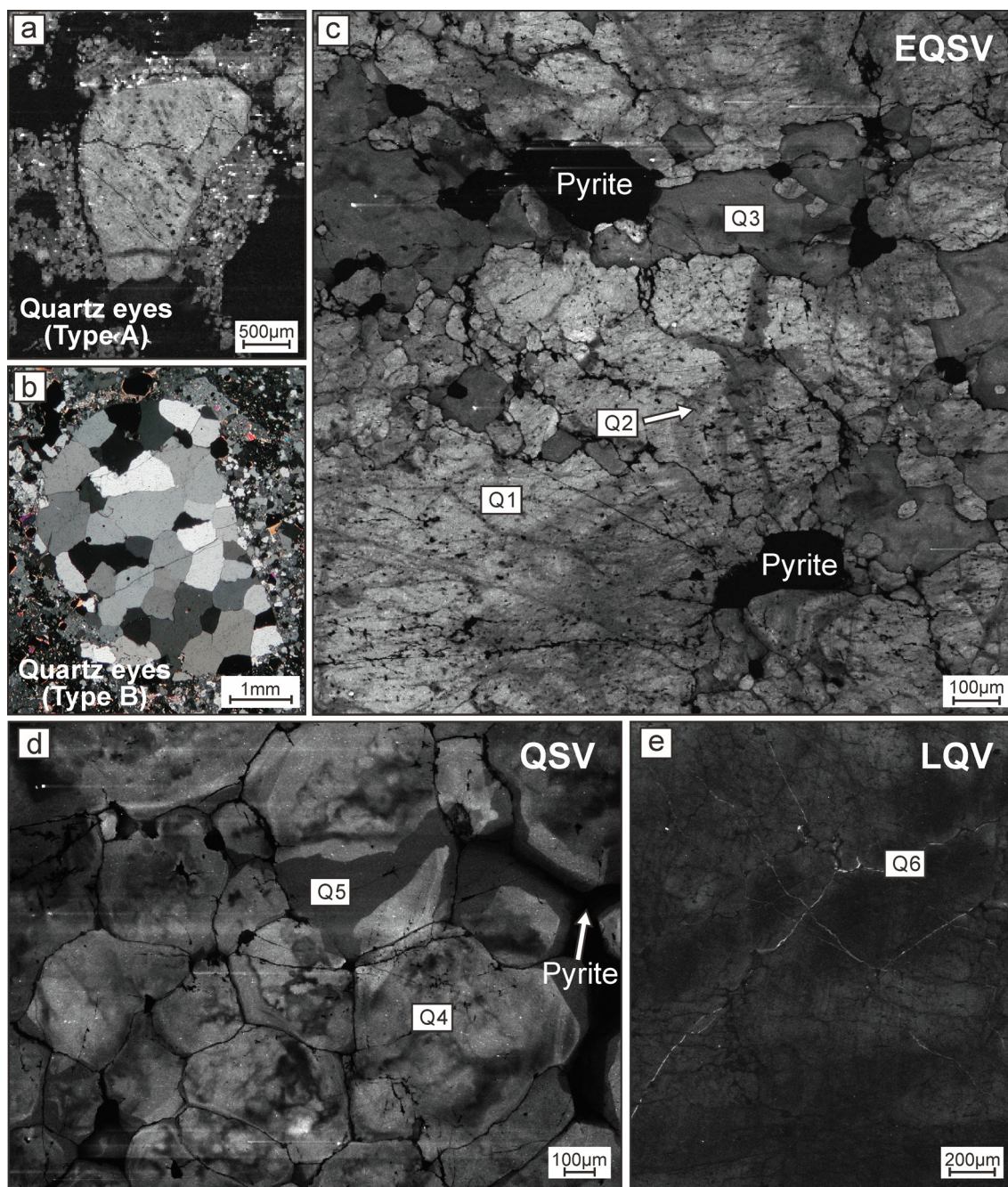
Fig. 4. SEM-CL photomosaics and microphotographs under crossed polarized light, showing the petrographic characteristics of successive quartz generations in the different vein stages. (a) CL image of anhedral quartz eyes (Type A), showing CL-gray color with no obvious oscillatory zoning; (b) Sugary aggregated of anhedral quartz eyes (Type B) under crossed polarized light; (c) CL image of early quartz-sulfide veins, there are three different quartz generations, and the earliest formed quartz (Q1) with relative bright color and later CL-gray quartz (Q2 and Q3); (d) CL image of quartz-sulfide veins, the vein is composed of sugary anhedral quartz (Q4) with dark color and filled by later quartz (Q5); (e) CL image of late quartz veins, showing the vein quartz (Q6) has dark color and no other types of quartz developed. EQSV = early quartz-sulfide veins, QSV = quartz-sulfide veins, LQV = late quartz veins.

5.4. Raman microspectroscopy

From the magmatic-hydrothermal transitional stage to the hydrothermal stage, we obtained over 50 fluid and melt inclusions results and all Raman spectroscopy results were referred to Frezzotti et al. (2012). Figs. 5 and 6 show the Raman spectroscopy results. Fluid inclusions in the quartz eyes have an H_2O-rich and micro-CH_4 vapor phase. The M1 and M2 inclusions have only H_2O or N_2-bearing vapor phase. In addition, fluid inclusions from EQSV and QSV include $H_2O + CH_4$ only, with a notable absence of CO_2. In the fluid inclusions of some QSV, we detected abundant CH_4 with micro-N_2 in the vapor phase. In most fluid inclusions in the LQV, we detected $H_2O + CH_4$ and CO_2. The opaque daughter minerals have been identified as pyrite and chalcopyrite in quartz eyes (Type A) and EQSV.

5.5. He–Ar isotopes

Supplementary Table 3 lists He and Ar isotopic compositions measured in this study. The ^4He concentrations vary from 2.43×10^{-8} to 29.9×10^{-8} cc STP/g. The ^{40}Ar concentrations range between 2.25×10^{-8} and 22.7×10^{-8} cc STP/g. The $^3He/^4He$ and $^{40}Ar/^{36}Ar$ ratios range from 0.11 to 0.96 Ra and 418.7–2920.2, respectively.
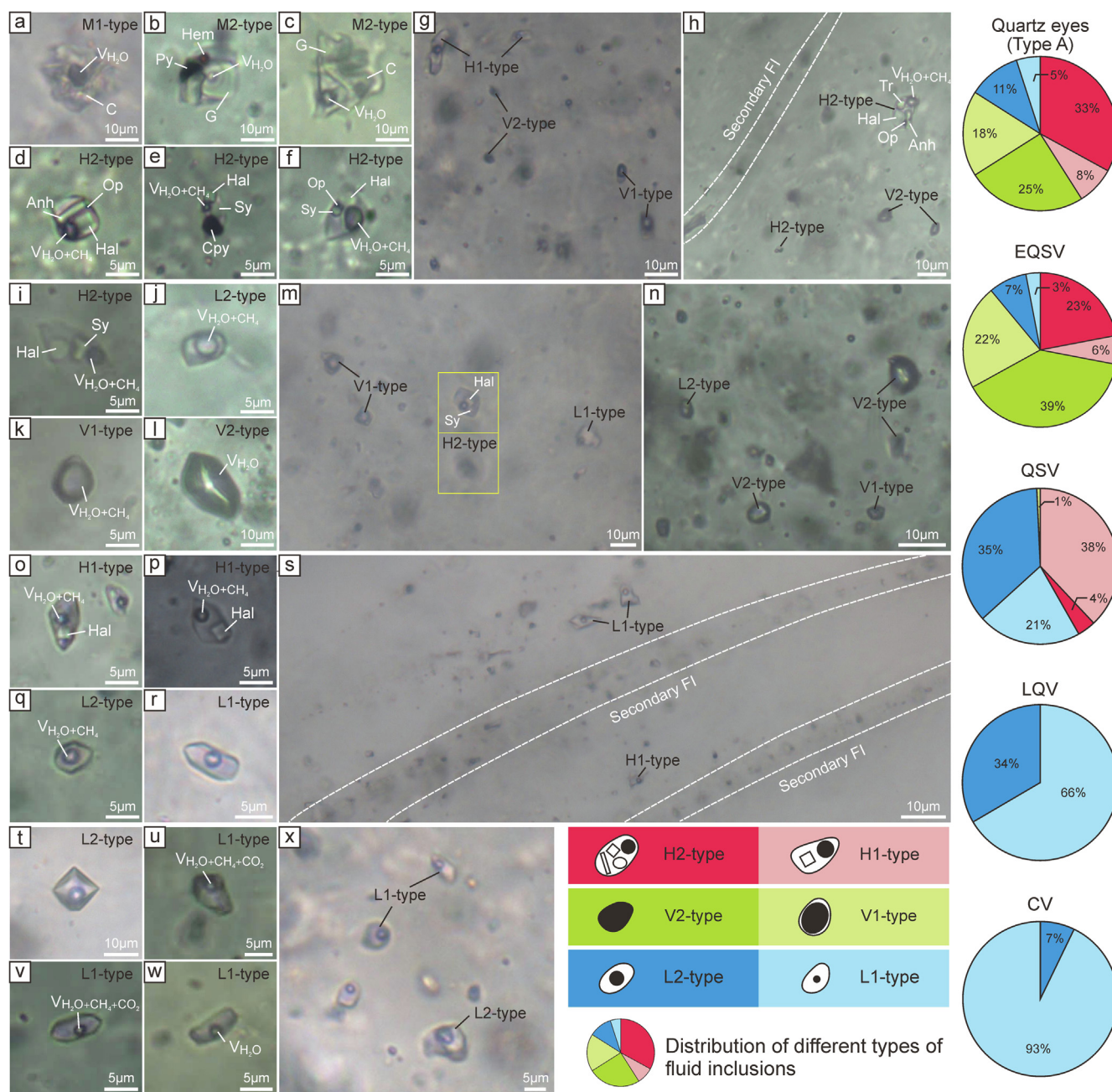
Fig. 5. Photomicrographs of representative fluid inclusions and distribution of different types of fluid inclusions. (a–h) Different types of fluid inclusions in quartz eyes (Type A); (i–n) Different types of fluid inclusions in EQSV veins; (o–s) Different types of fluid inclusions in QSV veins; (t–x) Different types of fluid inclusions in LQV veins. EQSV = early quartz-sulfide veins, QSV = quartz-sulfide veins, LQV = late quartz veins. M1 type = melt inclusions, M2 type = melt-fluid inclusion, Hem = hematite, Py = pyrite, Cpy = chalcopyrite, Anh = anhydrite, C = crystallized melt inclusions, G = glassy melt inclusions, Op = opaque minerals, Tr = unknown transparent mineral, Hal = halite, Sy = sylvite.

5.6. C–H–O isotopes

We measured hydrogen and oxygen isotopic compositions of quartz from the EQSV, QSV, and LQV, where the measured δD and δ^{18}O ranged from −106.0 to −89.9‰ and 9.7 to 12.1‰, respectively (Supplementary Table 4). Based on these results, and assuming that mineral deposition occurred under isotope equilibrium with an aqueous fluid, we calculated δ^{18}O$_{H2O}$ using the respective measured homogenization temperatures and the oxygen isotope fractionation factors in the quartz–H$_2$O system (Clayton et al., 1972). The computed δ^{18}O$_{H2O}$ values range from −1.8 to +5.2‰. Carbon isotopes were measured in the extracted bulk inclusion fluids in quartz from the QSV, which yielded δ^{13}C$_{fluid}$ values from −26.3 to −28.5‰ (Supplementary

Table 5).

5.7. whole-rock organic carbon contents and isotope

The organic carbon contents of the carbonaceous slate and shale samples are from 0.14 to 5.75 wt%, and their organic carbon isotopic compositions range from −28.24 to −32.39‰ (Supplementary Table 6).
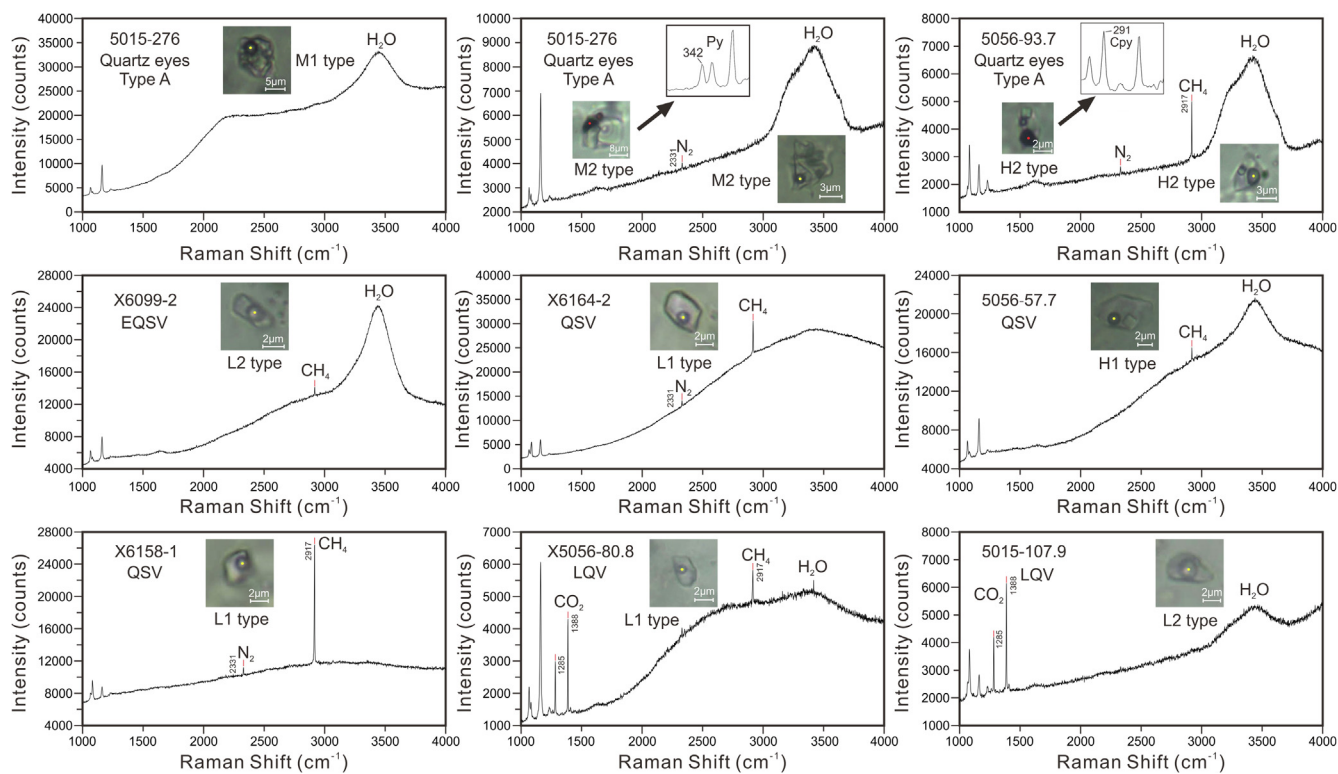
Fig. 6. Laser Raman spectra of fluid inclusions from the No.1 deposit in the Xiongcun district. Py = pyrite, Cpy = chalcopyrite, EQSV = early quartz-sulfide veins, QSV = quartz-sulfide veins, LQV = late quartz veins.

6. Discussion

6.1. Sources of the ore-forming fluid

6.1.1. He–Ar isotope evidence

He and Ar isotopic compositions of mineralizing fluids provide a powerful tool to trace crustal and mantle contribution associated with ore-forming processes (Turner et al., 1993; Stuart et al., 1994). Noble gases trapped in fluid inclusions have three potential sources, i.e., air-saturated water, mantle, and crust (Turner et al., 1993).

Generally, He in ore-forming fluids has only two sources, which includes the mantle and the crust because the amount of He in the atmosphere is insignificant and does not influence the He isotopic composition of most crustal fluids (Marty et al., 1989; Stuart et al., 1994). The $^3He/^{36}Ar$ ratios of the analyzed samples range from 9.32 to 129.22×10^{-5}, which is three orders of magnitude higher than air-saturated water (approximately 5×10^{-8}). This is consistent with the F^4He (> 2728, average = 8832) values, which suggests that ^4He in these samples is more than 2.728 times enriched compared with atmospheric concentrations. The $^3He/^4He$ ratios (0.11–0.96 Ra) for the ore-forming fluids from the No. 1 deposit are much higher than crustal ratios (0.01–0.05 Ra, Mamyrin and Tolstikhin, 1984; Turner et al., 1993) but lower than mantle ratios (6–9 Ra, Dunai and Baur, 1995; Gautheron and Moreira, 2002), and all samples plotted in the traditional field between crust helium and mantle helium (Fig. 7a), which demonstrates that the ore-forming fluids contain both mantle- and crustal-derived He. We estimated the proportion of mantle ^4He from the He mantle (%) = $(R_S - R_C)/(R_M - R_C) \times 100$, where $R_M = 8$, $R_C = 0.01$, and R_S represents the $^3He/^4He$ ratios of the fluids in the mantle, crust, and sample, respectively (Kendrick et al., 2001). The results yield relatively low He mantle values (1.25–11.9%). Thus, the low $^3He/^4He$ values in the sulfide-hosted fluid inclusions suggest that the ore-forming fluids derive predominantly from crustal fluids with a trace amount of mantle fluids. Similarly, on the ^3He vs. ^4He diagram (Fig. 7b), samples plotted between the mantle and crustal He domains,

suggesting that crustal He was a larger component in the ore-forming fluids.

Mantle-derived fluids are rich in ^3He and poor in ^{36}Ar (Turner et al., 1993), and $^{40}Ar/^{36}Ar$ sample ratios (418.7–2920.2) are higher than atmosphere ratios (295.5, Kendrick et al., 2001), which suggests atmosphere involvement and a significantly more radiogenic ^{40}Ar composition. According to the method proposed by Kendrick et al. (2001), we can estimate the radiogenic ^{40}Ar composition ($^{40}Ar^*\% = (1–295.5/(^{40}Ar/^{36}Ar)_{sample}) \times 100$). The results show that more than 57% (average value) of the $^{40}Ar/^{36}Ar$ values derive from the mantle or crustal sources. In summary, the compositions of He–Ar isotope indicate that the ore-forming fluid mainly derived from crust source with minor mantle input.

6.1.2. H–O isotope evidence

The H–O isotopic compositions provide information on the source of the ore-forming fluids. The $\delta^{18}O$ and δD isotopic data measured in this study generally plot between the magmatic field and meteoric water line (Fig. 8), which indicates that the ore-forming fluids have a magmatic-meteoric origin. However, the δD values from EQSV and QSV samples are much lower than the magmatic water values. Low δD values are likely a consequence of magma degassing (single-phase fluid exsolved and separated from primary magma chamber) and fluid boiling (single-phase fluid separated into two fluid phases) in most porphyry deposits (e.g., Nabelek et al., 1983; Giggenbach, 1992; Rust et al., 2004; Harris et al., 2005). Previous studies have shown that D, relative to H, preferentially fractionates into the vapor phase (Dobson et al., 1989; Horita et al., 1995). The vapor phase begins to exsolve from the magma at the time of emplacement when the melt contains approximately 30% of crystals (Nabelek et al., 1983). Moreover, the coexistence of brine inclusions and vapor-rich inclusions in Quartz eyes (Type A) and EQSV suggested that fluid boiling occurred during magmatic-hydrothermal fluid evolution (Fig. 5). Therefore, δD values significantly decrease during magma degassing and later hydrothermal fluid boiling. In addition, some δD values are lower than samples in the
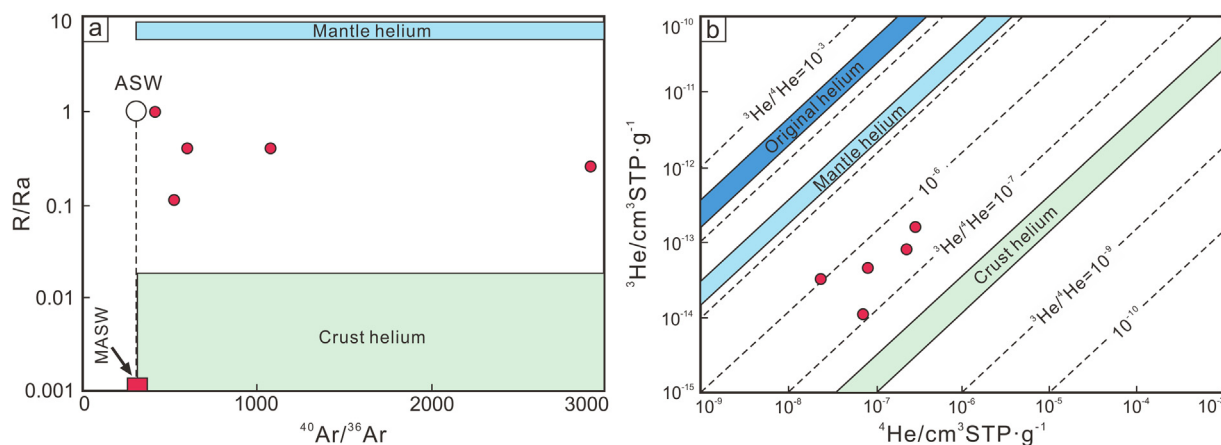
Fig. 7. (a) R/Ra–^{40}Ar–^{36}Ar and (b) ^{3}He–^{4}He plots of inclusion-trapped fluids in sulfide and quartz from the No.1 deposit in the Xiongcun district (Mamyrin and Tolstikhin, 1984; Winckler et al., 2001). ASW = air-saturated water; MASW = modified air-saturated water.
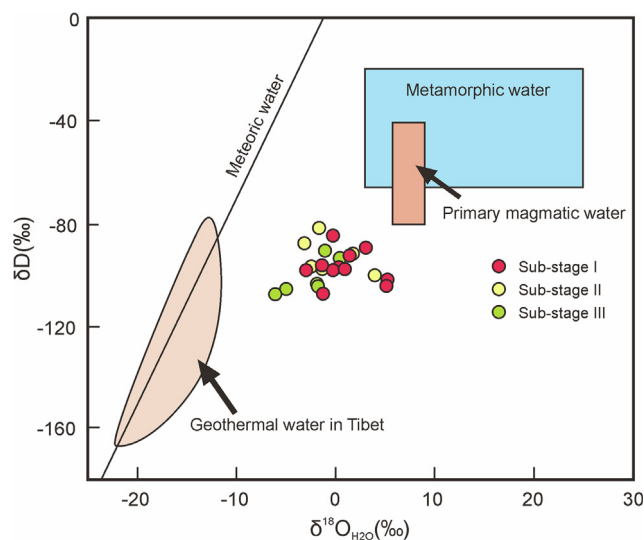

Fig. 8. Hydrogen and oxygen isotopic compositions of water, that in equilibrium with quartz from the No.1 deposit in the Xiongcun district. The primary magmatic and metamorphic water boxes are from Taylor (1974), the meteoric water line is from Zheng et al. (1983), and the geothermal water area is from Zheng et al. (1982).

same stage (Fig. 8). We speculate that this is because the bulk fluid inclusion decrepitation method, which was employed to provide the water for the δD_{H2O} analyses, inevitably led to sampling a mixture of primary and secondary fluid inclusions, resulting in low δD values.
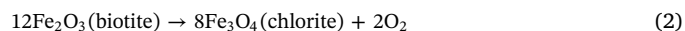
6.2. Magma and fluid oxygen fugacity

Oxygen fugacity (fO_2) exerts control on the metal partitioning behavior between ferromagnesian phases and melts, and may even restrict the development of a porphyry copper system (Richards, 2015). Based on the fO_2 data of No.1 deposit from Xie et al. (2018), the Ce^{4+}/Ce^{3+} ratios (average 175) of zircons reflect relatively high fO_2, although they are lower than other porphyry copper deposits, such as the Yulong (average 204) and Malasongduo porphyry Cu–Mo deposit (average 258, Liang et al., 2006). On the basis of the formula to estimate the log fO_2, found in Trail et al. (2012), and the magma crystallization temperature via the Ti-in-zircon thermometry (after Watson et al., 2006; Ferry and Watson, 2007), we calculated an average log fO_2 values of −15 at 645 °C (> NNO, Supplementary Table 7). Moreover, hematite was observed in the melt-fluid inclusions (Fig. 5b), which proves that magma crystallization occurred under high fO_2 conditions (Parat et al., 2011).

Finally, we infer that the magma of the mineralized quartz diorite porphyry was oxidized and estimate its redox condition to be at log fO_2 > NNO. This fO_2 is similar to the previously recognized lower limit for most copper porphyries (FMQ + 2, Mungall, 2002).

As noted above, the primary magma is characterized by high fO_2 values (> NNO); however, the oxygen fugacity has significantly changed in the subsequent hydrothermal stages. We confirm that CH_4 ($CH_4 \gg CO_2$) exists in the quartz eyes (Type A) (Fig. 6), i.e., fO_2 should be lower than the FMQ oxygen buffer in the early hydrothermal stages (Takagi and Tsukimura, 1997). However, an unusual phenomenon revealed fO_2 of the hydrothermal fluid in the early hydrothermal stage is variable and unstable: anhydrite crystals were captured in the CH_4-rich fluid inclusion under inhomogeneous conditions (Fig. 5d, h). In general, anhydrite occurs as a stable phase in the early hydrothermal stage at fO_2 values greater than or equal to log fO_2 units above NNO (ΔNNO ≥ 1.0–1.5, Carroll and Rutherford, 1987). This means anhydrite and CH_4-rich fluid cannot co-exist within a homogeneous and stable hydrothermal system. Additionally, we did not identify CH_4 in the melt-fluid/melt inclusions (Fig. 5a–c), which is also illustrated by the absence of CH_4 in primary fluid exsolved from the magma. Thus, we presume that the addition of CH_4 could change the hydrothermal fluid from an oxidized to a reduced condition (explained below).

In the subsequent hydrothermal stage, CH_4 was widely distributed in the hydrothermal fluid, and we observe abundant CH_4-rich fluid inclusions in some QSV. To some extent, this phenomenon can be explained by the mineral assemblage, i.e., abundant pyrrhotite (Table 1) growth in sub-stage I and II, which shows that the fluid fO_2 is below the FMQ buffer. During sub-stage III, the gradual transfer of CO_2 contents to the LQV suggests that the fluid fO_2 had an increasing trend and that the fO_2 could be above the FMQ buffer if the condition, $CH_4 \ll CO_2$, is met in the CO_2–CH_4–H_2O system (Takagi and Tsukimura, 1997). This transitional process is illustrated by biotite chloritization (Supplementary Fig. 3c, Tarantola et al., 2007, 2009):

$$CH_4 + 2O_2 \rightarrow CO_2 + 2H_2O \tag{1}$$

$$12Fe_2O_3 (biotite) \rightarrow 8Fe_3O_4 (chlorite) + 2O_2 \tag{2}$$

$$CH_4 + 12Fe_2O_3 (biotite) \rightarrow CO_2 + 8Fe_3O_4 (chlorite) + 2H_2O \tag{3}$$

6.3. CH$_4$ produced via the thermogenic process

The origin of CH_4 is the key issue when attempting to trace the processes that initiate the transition from oxidized to reduced conditions. Generally, the principal sources of CH_4 can be classified into four groups: (1) mantle (directly derived from the mantle or subduction dehydration processes, Sugisaki and Mimura, 1994; Beeskow et al.,

2006), (2) biogenic (produced by microbial processes, Whiticar 1999; Ueno et al., 2006), (3) abiogenic synthesis via the Fischer-Tropsch type (FTT, Konnerup et al., 1985; Nivin et al., 2005; Fiebig et al., 2009), and (4) thermogenic (thermal decomposition of organic matter, Whiticar, 1999; Bréas et al., 2001).

The measured $\delta^{13}C_{fluid}$ values (-26.3 to -28.5‰) are the total carbon composition of the fluid, which can approximately represent the $\delta^{13}C_{CH_4}$ values because the fluid mainly consists of CH_4 rather than CO_2 or other C-compounds based on Raman spectroscopy analyses (Fig. 6). Firstly, we can exclude a biogenic process origin. The measured $\delta^{13}C_{CH_4}$ values are enriched in ^{13}C more than typical biologically produced CH_4 ($\delta^{13}C_{CH_4} < -60$‰, Schoell, 1988). Previously published S isotopic data ($\delta^{34}S = -3.5$ to $+1.79$‰, Tang et al., 2015) indicate a typical magmatic source rather than a biological source. Secondly, the $\delta^{13}C_{CH_4}$ values in the No. 1 deposit are lower than mantle values (-25 to -15‰, Carapezza and Federicob, 2000; Taran et al., 2001, 2002a), and the gas in the mantle also has a high $^3He/^4He$ ratio (6–8 Ra, Taran et al., 2002b, Farley and Neroda, 1998) relative to the No. 1 deposit (0.11–0.96 Ra). In the majority of the hydrothermal-dominated systems, abiogenically produced CH_4 gas is connected to FTT reactions (e.g., Nivin et al., 2005; Fiebig et al., 2009). In general, the geochemical criterion to identify an FTT reaction is $\delta^{13}C_{CH_4}$ values that are higher than -26‰ (Welhan, 1988; Ueno et al., 2006), but the $\delta^{13}C_{CH_4}$ values in the No. 1 deposit are lower than this value. In addition, CO_2 gas is not observed in the early hydrothermal stage.

Therefore, thermogenesis is the most likely explanation. There are many reasons to interpretation the CH_4 produced via thermogenic processes: (1) On δD_{CH_4} vs. $\delta^{13}C_{CH_4}$ diagram, all data plot near the thermogenic field, suggesting that CH_4 is produced by thermogenesis (Fig. 9). (2) Thermogenic hydrocarbons that derive from the thermal degradation of organic matter usually exhibit methane to ethane plus propane ratios smaller than 100 (Fiebig et al., 2009), which is compatible with the methane to ethane ratios at the No. 1 deposit that ranges from 1.7 to 17 (Xu et al., 2009). (3) Organic carbonaceous rocks mainly distribute in the northwest of the Xiongcun district at present, which belongs to the upper section of Xiongcun Formation (Lang et al., 2019a). These carbonousrous rocks may have been more widespread within the Xiongcun district during the Jurassic period, because the exhumation amounts for Xiongcun district are about 4–6 km since 20 Ma (Zhou et al., 2019). In addition, the Middle Jurassic quartz diorite porphyry intruded into the carbon-bearing wall rocks (Fig. 10) and the organic carbon contents of wall rocks are from 0.14 to 5.75%

(Supplementary Table 6), indicating they can apply enough carbon species to produce CH_4. (4) The thermogenic process of CH_4 is related to thermal ($> 150\,°C$) degradation of sedimentary organic matter (Whiticar, 1999; Bréas et al. 2001). The Ti-in-zircon thermometry indicates that the magma crystallization temperature is close to $700\,°C$, which is the approval of this process. (5) The carbon isotopic compositions of organic carbon from carbon-bearing wall rocks are consistent with those of fluid inclusions (Supplementary Table 6). Therefore, it is precise because of the thermogenic process that produced abundant CH_4, which contributed to the evolution of the porphyry copper system from oxidized to reduced conditions.

6.4. Metal deposition mechanisms

Fluid exsolution from the magma and fluid/melt immiscibility in porphyry copper system allow the preferential enrichment of ore-forming metals into the fluid phase (Lowenstern et al., 1991; Kamenetsky et al., 2003; Harris et al., 2003). As hydrothermal fluid ascent, the temperature and pressure further decrease. When the temperature and pressure are below the critical curve, a single-phase fluid may separate into two phases (low-salinity vapor and high-salinity liquid), which is also called fluid boiling. At No. 1 deposit, the coexistence of high salinity H1-, H2-type fluid inclusions and low salinity V1-, V2-type fluid inclusions in Quartz (Type A) and EQSV is well supported this process (Fig. 5g, h, m, n). In general, such volatile-rich vapors and high Cl concentration liquids have strong transportability for ore-forming metals, including Cu and Au (e.g., Hemley, 1992; Hemley and Hunt, 1992; Simon et al., 2005; Zajacz et al., 2010). With volatile concentrations within the cupola zones and the formation of open-standing brittle fracture, the fluid escapes from the intrusion and the pressure is decreasing (Burnham, 1979), which dramatically reduces the solubility of the metal-chloride species and causes deposition of metals (e.g., Crerar and Barnes, 1976; Landtwing et al., 2005; Klemm et al., 2007, Richards, 2011). The most significant piece of evidence for volatile-rich fluid flow and metal deposition during the early hydrothermal stage at the No. 1 deposit: (1) there are widespread occurrences of embayed quartz phenocrysts (quartz eye type A), miarolitic pods or cavities in the trapped bubbles (subsequently formed quartz eye type B), and vapor-rich inclusions in the EQSV veins, (2) abundant sulfides can be trapped in many brine inclusion (Fig. 5e, f, h), indicating metals have been precipitated during early hydrothermal stage. Therefore, we confirmed that ore elements deposit via fluid boiling as a consequence of the rapid decrease in temperature and pressure.

6.5. Evolution of CH_4-rich fluids in the magmatic-hydrothermal system

The quartz diorite porphyry (167–161 Ma) intruded into volcanic–sedimentary rocks of the Xiongcun Formation (195–165 Ma) and subsequently formed No. 1 porphyry Cu-Au deposit (Fig. 11). The evolution of CH_4-rich fluids in the magmatic-hydrothermal system is described below:

At the magmatic stage, at temperature near $700\,°C$, based on the Ti-in-zircon geothermometer (Xie et al., 2018), the quartz dioritic magma was characterized by a high fO_2 state ($>$ NNO). As magma quickly ascended, euhedral quartz phenocrysts were transported to shallow levels (Fig. 11a).

During the magmatic-hydrothermal transitional stage, as the magma temperature and pressure decreased, the water became saturated and separated from the silicate melt. A single phase separated into a vapor-rich (V1 and V2) and high-salinity liquid phase (H1 and H2) (Fig. 5; Supplement Table 2), and volatile-rich bubbles adsorbed quartz crystals and coalesced water bubbles. When the bubbles were caught in the melt, miarolitic cavities formed (Harris et al., 2004). These vapor-rich fluid inclusions (V1) have high homogenization temperatures of 421 to 471 °C and low salinities (5.7 to 8.8 wt% NaCl equiv), on the contrary, brine inclusions (H1 and H2) have relative low
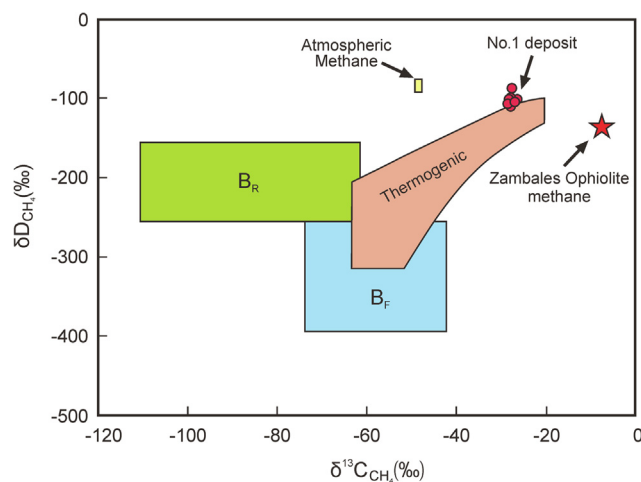

Fig. 9. Diagram of $\delta^{13}C$ vs. δD of CH_4 in the fluid inclusions from the No.1 deposit in the Xiongcun district (Schoell, 1988). B_R = Bacterial methane by CO_2 reduction, B_F = Bacterial methane by fermentation, Atmospheric methane (Wahlen et al., 1987), Zambales Ophiolite methane Philippines (Abrajano et al., 1988).
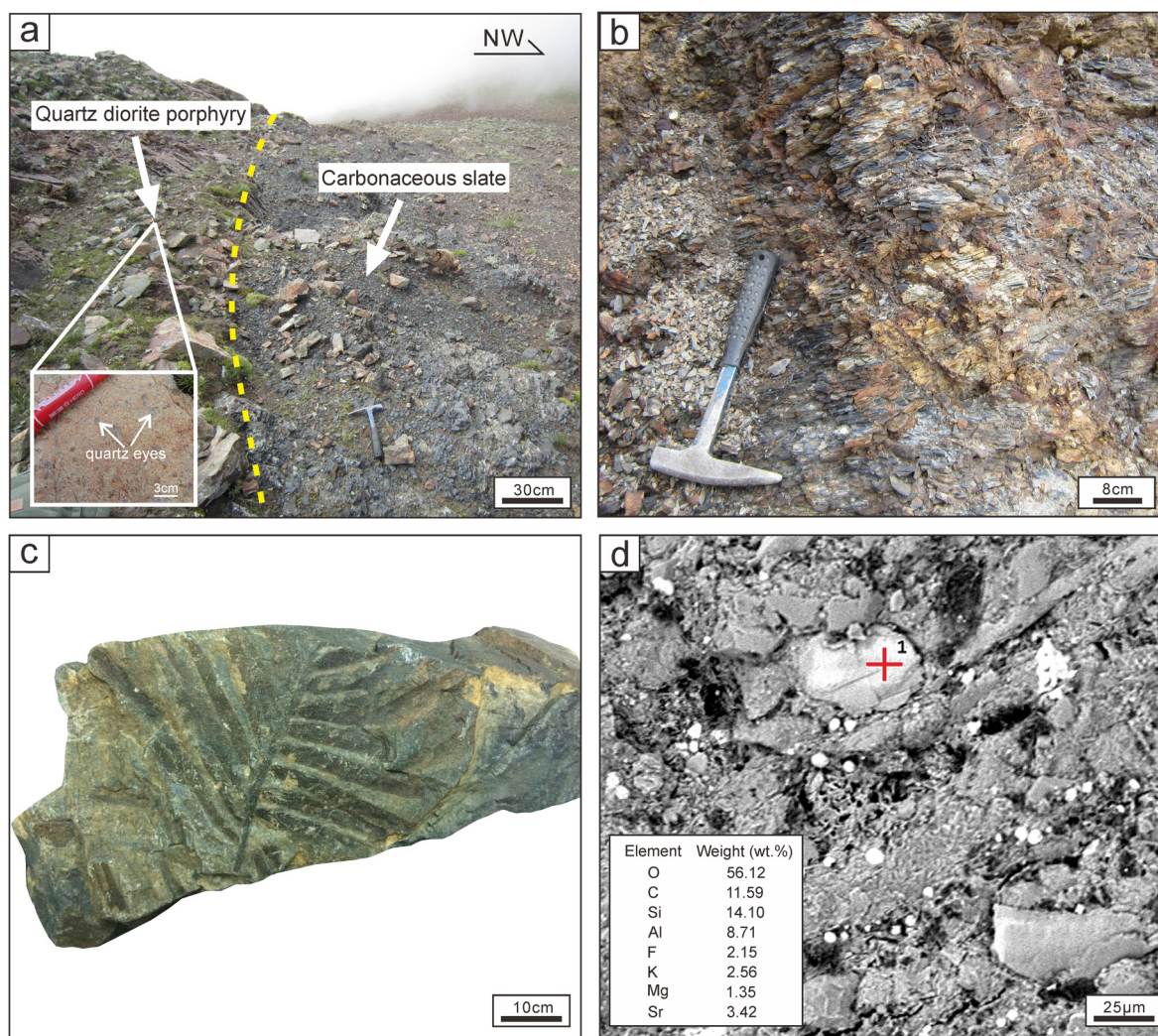
Fig. 10. Photographs are showing carbonaceous wall rocks in the Xiongcun district. (a) Quartz diorite porphyry intruded into the carbonaceous slate of Xiongcun Formation. (b) Photograph of carbonaceous shale. (c) Plant fossil (*Ptilophyllum* sp.) preserved in the siltstone of Xiongcun Formation. (d) SEM-EDS analytical results are showing carbonaceous material grains in carbonaceous shale.

homogenization temperatures of 271 to 440 °C and high salinities (35.9 to 62.8 wt% NaCl equiv). Meanwhile, magma ascent produced abundant CH_4 by heating the carbonaceous wall rocks. This process changed the porphyry copper system redox state from oxidized to reduced conditions (Fig. 11b).

In the hydrothermal stage, CH_4-rich fluid interacted with rocks (e.g., porphyry and tuff) and produced potassic alteration characterized by developed pyrrhotite and fluid with fO_2 below the FMQ buffer. With the rapid decrease in temperature and pressure, abundant ore-forming metals precipitated via fluid boiling in the potassic alteration zone. Compared to the magmatic-hydrothermal transitional stage, the brine inclusions (H1 and H2) vapor-rich fluid inclusions (V1) have low homogenization temperatures and salinities (274 to 422 °C; 3.2 to 58.4 wt% NaCl equiv). The addition of meteoric water and a change in the hydrothermal fluid redox produced pyrite–pyrrhotite–sphalerite assemblages and related veins (e.g., PV, CPPV, and PMV; Table 1) with minor mineralization. During the late hydrothermal stage, the homogenization temperatures and salinities of fluid inclusions significantly decrease (132 to 186 °C; 0.9 to 9.6 wt% NaCl equiv), and LQV and CV contain only liquid-rich fluid inclusions (L1 and L2). Additionally, biotite chloritization produced abundant CO_2, during which the fluid oxygen fugacity increased to above the FMQ buffer. Thus, the CH_4-dominated fluid transformed to a CH_4–CO_2-dominated fluid (Fig. 11c).

7. Conclusions

(1) The He–Ar isotopic compositions suggest that the ore-forming fluids predominantly derived from crust source with minor mantle input. The H–O isotopic analysis results indicate that the ore-forming fluids were derived from a magmatic source that mixed with some meteoric waters.

(2) CH_4 in hydrothermal fluid is a thermogenic origin, which was generated by the thermal decomposition of organic matter from the carbonaceous wall-rocks.

(3) Ore elements were deposited via fluid boiling as a consequence of the rapid decrease in temperature and pressure.

(4) The primary quartz diorite porphyry is characterized by high fO_2 values (> NNO). Subsequently, CH_4 added into the hydrothermal system, which contributed to the evolution of the porphyry copper system from oxidized to reduced conditions.
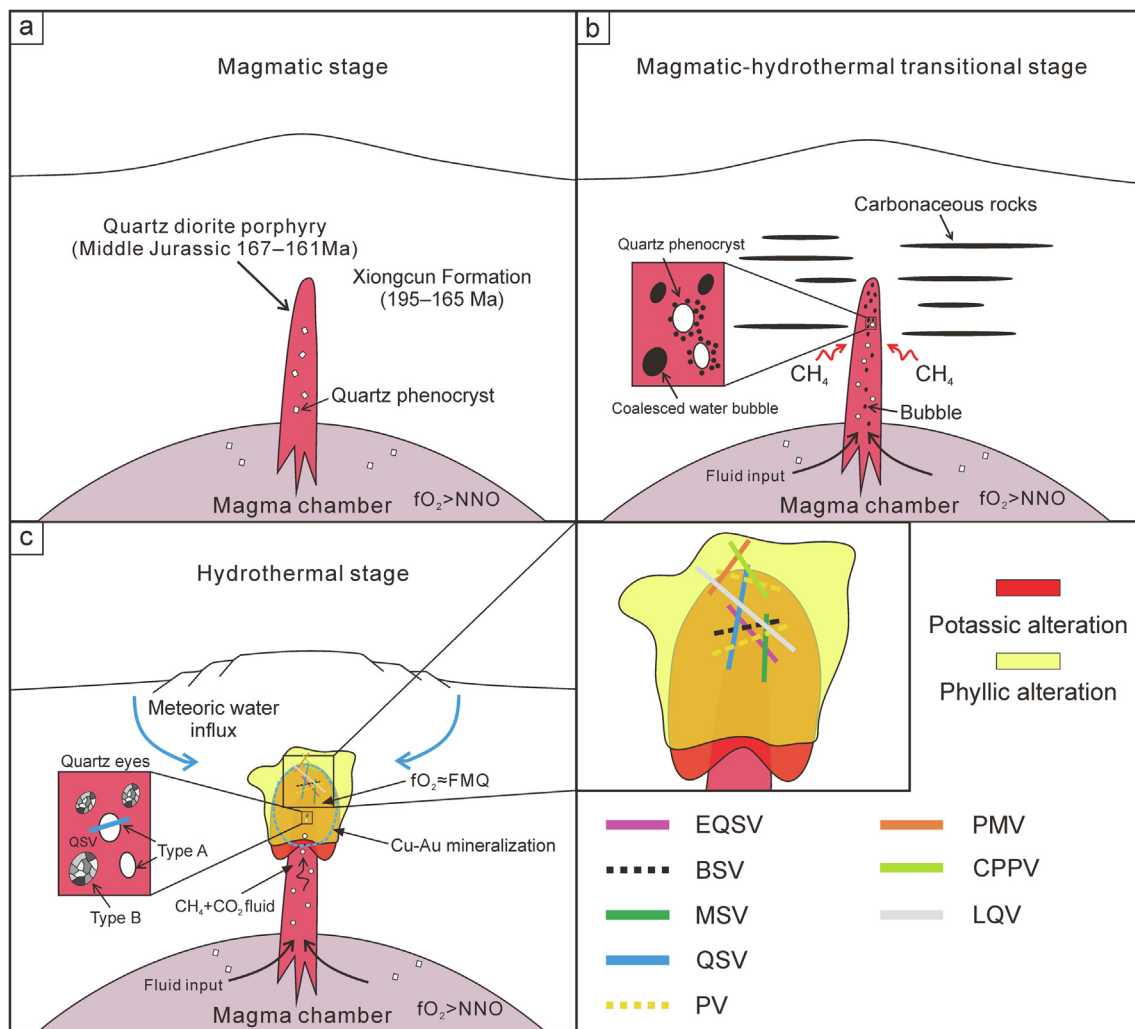
Fig. 11. Schematic diagrams depict the evolution of the magmatic-hydrothermal system in the No.1 deposit in the Xiongcun district. (a) Magmatic stage: Quartz diorite porphyry (fO_2 > NNO) emplaced in Xiongcun Formation at shallow levels and brought abundant euhedral quartz phenocrysts from magma chamber to location of emplacement. (b) Magmatic-hydrothermal transitional stage: Fluid exsolution from the quartz diorite porphyry magma, caused phase separation. Volatile-rich vapor transport along the low pressure tracks to the roof of porphyry, and resorbed quartz phenocrysts and coalesced water bubbles. Meanwhile, CH_4 have been produced by heating carbonaceous wall rocks. (c) Hydrothermal stage: With the decrease of temperature and pressure, abundant ore-forming metals precipitated via fluid boiling in early potassic alteration. Bubbles previously formed cavities and filled by later hydrothermal fluid, presented two different types of quartz eyes. The addition of meteoric water and a change in the hydrothermal fluid redox developed various veins and mineral assemblages.

Appendix A. Supplementary data

Supplementary data to this article can be found online at https://doi.org/10.1016/j.oregeorev.2019.103212.

References

Abrajano, T.A., Sturchio, N.C., Bohlke, J.K., Lyon, G.L., Poreda, R.J., Stevens, C.M., 1988. Methane–hydrogen gas seeps, Zambales ophiolite, Philippines: deep or shallow origin? Chem. Geol. 71, 211–222.

Beeskow, B., Treloar, P.J., Rankin, A.H., Vennemann, T.W., Spangenberg, J., 2006. A reassessment of models for hydrocarbon generation in the Khibiny nepheline syenite complex, Kola Peninsula, Russia. Lithos 91, 1–18.

Bréas, O., Guillou, C., Reniero, F., Wada, E., 2001. The global methane cycle: isotopes and mixing ratios, sources and sinks. Isot. Environ. Health Stud. 37, 257–379.

Burnham, C.W., 1979. Magmas and hydrothermal fluids. In: Barnes, H.L. (Ed.), Geochemistry of Hydrothermal Ore Deposits, second ed. Wiley, New York, pp. 71–136.

Candela, P.A., Blevin, P.L., 1995. Do some miarolitic granites preserve evidence of magmatic volatile phase permeability? Econ. Geol. 90, 2310–2316.

Cao, M.J., Qin, K.Z., Li, G.M., Jin, L.Y., Evans, N.J., Yang, X.R., 2014a. Baogutu: an example of reduced porphyry Cu deposit in western Junggar. Ore Geol. Rev. 56, 159–180.

Cao, M.J., Qin, K.Z., Li, G.M., Evans, N.J., Jin, L.Y., 2014b. Abiogenic Fischer-Tropsch synthesis of methane at the Baogutu reduced porphyry copper deposit, western Junggar, NW-China. Geochim. Cosmochim. Acta 141, 179–198.

Cao, M.J., Qin, K.Z., Li, G.M., Evans, N.J., Hollings, P., Maisch, M., Kappler, A., 2017. Mineralogical evidence for crystallization conditions and petrogenesis of ilmenite-series I-type granitoids at the Baogutu reduced porphyry Cu deposit (Western Junggar, NW China): Mössbauer spectroscopy, EPM and LA-(MC)-ICPMS analyses. Ore Geol. Rev. 86, 382–403.

Carapezza, M.L., Federicob, C., 2000. The contribution of fluid geochemistry to the volcano monitoring of Stromboli. J. Volcanol. Geothermal Res. 95, 227–245.

Carroll, M.R., Rutherford, M.J., 1987. The Stability of igneous anhydrite: experimental results and implications for sulfur behavior in the 1982 El chichon trachyandesite and other evolved magmas. J. Petrol. 28, 781–801.

Chang, Z.S., Meinert, L.D., 2004. The magmatic-hydrothermal transition–evidence from quartz phenocryst textures and endoskarn abundance in Cu-Zn skarns at the Empire Mine, Idaho. USA. Chem. Geol. 210, 149–171.

Chen, R., Liu, Y.L., Guo, L.S., Wang, Z.H., Liu, H.F., Xu, K.F., Zhang, J.S., 2014. Geochronology and Geochemistry of the Tinggong Porphyry Copper Ore Deposit, Tibet. Acta Geol. Sin. (English Edition) 88, 780–800.

Chen, Y., Tang, J.X., Sun, C.M., Lang, X.H., Huang, Y., 2008. A discussion on the alteration features and genesis of the Xiongcun Cu(Au) deposit in Xietongmen County,

Tibet, China. J. Chengdu Univ. Technol. (Sci Technol. Ed.) 35 (3), 303–308 (in Chinese with English abstract).

Clayton, R.N., O'Neil, J.R., Mayeda, T.K., 1972. Oxygen isotope exchange between quartz and water. J. Geophys. Res. 77, 3057–3067.

Cooke, D.R., Hollings, P., Walshe, J.L., 2005. Giant porphyry deposits: characteristics, distribution, and tectonic controls. Econ. Geol. 100, 801–818.

Crerar, D.A., Barnes, H.L., 1976. Ore solution chemistry V. Solubilities of chalcopyrite and chalcocite assemblages in hydrothermal solution at 200 °C to 350 °C. Econ. Geol. 71, 772–794.

Dobson, P.F., Epstein, S., Stolper, E.M., 1989. Hydrogen isotope fractionation between coexisting vapor and silicate glasses and melts at low pressure. Geochim. Cosmochim. Acta 53, 2723–2730.

Dunai, T.J., Baur, H., 1995. Helium, neon and argon systematics of the European sub-continental mantle: implications for its geochemical evolution. Geochim. Cosmochim. Acta 59, 2767–2784.

Farley, K.A., Neroda, E., 1998. Noble gases in the earth's mantle. Annu. Rev. Earth Planet. Sci. 26 (1), 189–218.

Ferry, J.M., Watson, E.B., 2007. New thermodynamic models and revised calibrations for the Ti-in-zircon and Zr-in-rutile thermometers. Contrib. Miner. Petrol. 154, 429–437.

Fiebig, J., Woodland, A.B., Alessandro, W.D., Püttmann, W., 2009. Excess methane in continental hydrothermal emissions is abiogenic. Geology 37, 495–498.

Frezzotti, M.L., Tecce, F., Casagli, A., 2012. Raman spectroscopy for fluid inclusion analysis. J. Geochem. Explor. 112 (1), 1–20.

Fu, Q., Xu, B., Zheng, Y.C., Yang, Z.S., Hou, Z.Q., Huang, K.X., Liu, Y.C., Zhang, C., Zhao, L., 2017. Two episodes of mineralization in the Mengya'a deposit and implications for the evolution and intensity of Pb-Zn-(Ag) mineralization in the Lhasa terrane, Tibet. Ore Geol. Rev. 90, 877–896.

Gautheron, C., Moreira, M., 2002. Helium signature of the subcontinental lithospheric mantle. Earth Planet. Sci. Lett. 199, 39–47.

Giggenbach, W.F., 1992. Isotopic shifts in waters from geothermal and volcanic systems along convergent plate boundaries and their origin. Earth Planet. Sci. Lett. 113, 495–510.

Goldstein, R.H., Reynolds, T.J., 1994. Systematics of fluid inclusions in diagenetic minerals: Society of Sedimentary Geology. SEPM Short Course 31, 199.

Hall, D.L., Sterner, S.M., Bodner, R.J., 1988. Freezing point depression of NaCl-KCl-H2O solution. Econ. Geol. 83, 197–202.

Harris, A.C., Kamenetsky, V.S., White, N.C., Achterbergh, V.E., Ryan, C.G., 2003. Silicate-melt inclusions in quartz veins: linking magmas and porphyry Cu deposits. Science 302, 2109–2111.

Harris, A.C., Kamenetsky, V.S., White, N.C., Steele, D.A., 2004. Volatile phase separation in silicic magmas at Bajo de la Alumbrera porphyry Cu-Au deposit, NW Argentina. Resour. Geol. 54, 341–356.

Harris, A.C., Golding, S.D., White, N.C., 2005. Bajo de la Alumbrera copper–gold deposit: stable isotope evidence for a porphyry-related hydrothermal system dominated by magmatic aqueous fluids. Econ. Geol. 100, 863–886.

Hedenquist, J.W., Lowenstern, J.B., 1994. The role of magmas in the formation of hydrothermal ore deposits. Nature 370, 519.

Hemley, J.J., 1992. Hydrothermal ore-forming processes in the light of studies in rock-buffered systems: I. Fe-Cu-Zn-Pb sulfide solubility relations. Econ. Geol. 87 (1), 1–22.

Hemley, J.J., Hunt, J.P., 1992. Hydrothermal ore-forming processes in the light of studies in rock-buffered systems; II. Some general geologic applications. . Econ. Geol. 87 (1), 23–43.

Horita, J., Cole, D.R., Wesolowski, D.J., 1995. The activity–composition relationship of oxygen and hydrogen isotopes in aqueous salt solutions: III. Vapor–liquid water equilibration of NaCl solutions to 350°C. Geochim. Cosmochim. Acta 59, 1139–1151.

Hou, Z.Q., Yang, Z.M., Qu, X.M., Meng, X.J., Li, Z.Q., Beaudoin, G., Rui, Z.Y., Gao, Y.F., Zaw, K., 2009. The Miocene Gangdese porphyry copper belt generated during post-collisional extension in the Tibetan Orogen. Ore Geol. Rev. 36, 25–51.

Huang, Y., Ding, F., Tang, J.X., Zhang, L., Lang, X.H., 2012. Genetic Mineralogy of Andalusite in Xiongcun Porphyry Copper-Gold Ore deposit, Tibet. Acta Geosci. Sin. 33 (4), 510–518 (in Chinese with English abstract).

Jahns, R.H., Burnham, C.W., 1969. Experimental studies of pegmatite genesis; l, A model for the derivation and crystallization of granitic pegmatites. Econ. Geol. 64, 843–864.

Kamenetsky, V.S., Vivo, B.D., Naumov, V.B., Kamenetsky, M.B., Mernagh, T.P., Achterbergh, E.V., Ryan, C.G., Davidson, P., 2003. Magmatic inclusions in the search for natural silicate-salt melt immiscibility: methodology and example. Dev. Volcanol. 5, 65–82.

Kang, Z.Q., Xu, J.F., Wilde, S.A., Feng, Z.H., Chen, J.L., Wang, B.D., Fu, W.C., Pan, H.B., 2014. Geochronology and geochemistry of the Sangri Group Volcanic Rocks, Southern Lhasa Terrane: Implications for the early subduction history of the Neo-Tethys and Gangdese Magmatic Arc. Lithos 200–201, 157–168.

Kendrick, M.A., Burgess, R., Pattrick, R.A.D., Turner, G., 2001. Fluid inclusion noble gas and halogen evidence on the origin of Cu-porphyry mineralizing fluids. Geochim. Cosmochim. Acta 65, 2651–2668.

Klemm, L.M., Pettke, T., Heinrich, C.A., Campos, E., 2007. Hydrothermal evolution of the El Teniente deposit, Chile: porphyry Cu–Mo ore deposit from low-salinity magmatic fluids. Econ. Geol. 102, 1021–1045.

Konnerup, M.J., Dubessy, J., Rose, H.J., 1985. Combined Raman microprobe spectrometry and microthermometry of fluid inclusions in minerals from igneous rocks of the Gardar province (south Greenland). Lithos 18, 271–280.

Landtwing, M.R., Pettke, T., Halter, W.E., Heinrich, C.A., Redmond, P.B., Einaudi, M.T., Kunze, K., 2005. Copper deposition during quartz dissolution by cooling magmatic–hydrothermal fluids: the Bingham porphyry. Earth Planet. Sci. Lett. 235, 229–243.

Lang, X.H., Tang, J.X., Li, Z.J., Huang, Y., Chen, Y., Zhang, L., 2011. Alteration and mineralization of No. I ore body in Xiongcun porphyry copper-gold metallogenic ore district , Xietongmen County , Tibet. Miner. Deposits 30 (2), 327–338 (in Chinese of English abstract).

Lang, X.H., Tang, J.X., Li, Z.J., Huang, Y., Ding, F., Yang, H.H., Xie, F.W., Zhang, L., Wang, Q., Zhou, Y., 2014a. U-Pb and Re–Os geochronological evidence for the Jurassic porphyry metallogenic event of the Xiongcun district in the Gangdese porphyry copper belt, southern Tibet, PRC. J. Asian Earth Sci. 79, 608–622.

Lang, X.H., Tang, J.X., Xie, F.W., Li, Z.J., Huang, Y., Ding, F., Yang, H.H., Zhou, Y., Wang, Q., 2014b. Geochronology and Geochemistry of the Southern Porphyry in the Xiongcun District, Tibet and its Geological Implications. Geotect. Metall. 38 (3), 609–620 (in Chinese with English abstract).

Lang, X.H., Tang, J.X., Yin, Q., Cui, Z.W., Huang, Y., Zhang, J.S., Gao, Y.M., Li, Z.J., Ding, F., Xie, F.W., Yang, Z.Y., Zeng, M., 2017. Geochemistry and genesis of Eocene Lamprophyres in the Xiongcun porphyry copper-gold district, southern margin of the Lhasa terrane, Tibet, China. Geochem. J. 51, 123–142.

Lang, X.H., Wang, X.H., Tang, J.X., Deng, Y.L., Cui, Z.W., Yin, Q., Xie, F.W., 2018. Composition and age of Jurassic diabase dikes in the Xiongcun porphyry copper–gold district, southernmargin of the Lhasa terrane, Tibet, China: petrogenesis and tectonic setting. Geol. J. 53, 1973–1993.

Lang, X.H., Liu, D., Deng, Y.L., Tang, J.X., Wang, X.H., Yang, Z.Y., Cui, Z.W., Feng, Y.X., Yin, Q., Xie, F.W., Huang, Y., Zhang, J.S., 2019a. Detrital zircon geochronology and geochemistry of Jurassic sandstones in the Xiongcun district, southern Lhasa sub-terrane, Tibet, China: implications for provenance and tectonic setting. Geol. Mag. 156 (4), 683–701.

Lang, X.H., Wang, X.H., Deng, Y.L., Tang, J.X., Xie, F.W., Zou, Y., Huang, Y., Li, Z., Yin, Q., Jiang, K., 2019b. Early Jurassic volcanic rocks in the Xiongcun district, southern Lhasa subterrane, Tibet: Implications for the tectono-magmatic events associated with the early evolution of the Neo-Tethys Ocean. Lithos 340–341, 166–180.

Lang, X.H., Guo, W.B., Wang, X.H., Deng, Y.L., Yang, Z.Y., Xie, F.W., Li, Z., Zhang, Z., Jiang, K., 2019c. Petrogenesis and tectonic implications of the ore-bearing porphyries in the Xiongcun district: Constraints from the geochronology and geochemistry. Acta Petrol. Sin. 35 (7), 2105–2123 (in Chinese with English abstract).

Lee, H.Y., Chung, S.L., Lo, C.H., Ji, J.Q., Lee, T.Y., Qian, Q., Zhang, Q., 2009. Eocene Neotethyan slab breakoff in southern Tibet inferred from the Linzizong volcanic record. Tectonophysics 477, 20–35.

Liang, H.Y., Campbell, I.H., Allen, C., Sun, W.D., Liu, C.Q., Yu, H.X., Xie, Y.W., Zhang, Y.Q., 2006. Zircon Ce^{4+}/Ce^{3+} ratios and ages for Yulong ore-bearing porphyries in eastern Tibet. Miner. Deposita 41, 152–159.

Liu, J.T., Yang, L.Q., Lu, L., 2013. Pulang reduced porphyry copper deposit in the Zhongdian area, Southwest China: constrains by the mineral assemblages and the ore-forming fluid compositions. Acta Petrol. Sin. 29, 3914–3924 (in Chinese with English abstract).

Lowenstern, J.B., Mahood, G.A., Rivers, M.L., Sutton, S.R., 1991. Evidence for extreme partitioning of copper into a magmatic vapor phase. Science 252, 1405–1409.

Mamyrin, B.A., Tolstikhin, I., 1984. Helium Isotopes in Nature. Elsevier, Amsterdam, pp. 267.

Marty, B., Jambon, A., Sano, Y., 1989. Helium isotope and CO2 in volcanic gases of Japan. Chem. Geol. 76, 25–40.

Mo, X.X., Zhao, Z.D., Deng, J.F., Dong, G.C., Zhou, S., Guo, T.Y., Zhang, S.L., Wang, L.L., 2003. Response of volcanism to the India-Asia collision. Earth Sci. Front. 10, 135–148 (in Chinese with English abstract).

Mungall, J.E., 2002. Roasting the mantle: slab melting and the genesis of major Au and Au-rich Cu deposits. Geology 30, 915–918.

Nabelek, P.I., O'Neil, J.R., Papike, J.J., 1983. Vapor phase exsolution as a controlling factor in hydrogen isotope variation in granitic rocks: the Notch Peak granitic stock, Utah. Earth Planet. Sci. Lett. 66, 137–150.

Nivin, V.A., Treloar, P.J., Konopleva, N.G., Ikorsky, S.V., 2005. A review of the occurrence, form and origin of C-bearing species in the Khibiny Alkaline Igneous Complex, Kola Peninsula, NW Russia. Lithos 85, 93–112.

Oliver, J., 2006. Geological mapping of the Xietongmen property and continuous areas, Tibet, PRC. Private Report to Continental Minerals Corp.

Pan, G.T., Mo, X.X., Zhu, D.C., Wang, L.Q., Li, G.M., Zhao, Z.D., Geng, Q.R., Liao, Z.L., 2006. Spatial-temporal framework of the orogenic belt and its evolution. Acta Petrol. Sin. 22, 521–533 (in Chinese with English abstract).

Parat, F., Holtz, F., Streck, M.J., 2011. Sulfur-bearing magmatic accessory minerals. Rev. Mineral. Geochem. 73, 285–314.

Richards, J.P., 2003. Tectonomagmatic precursors for porphyry Cu-(Mo-Au) deposit formation. Econ. Geol. 98, 1515–1533.

Richards, J.P., 2011. Magmatic to hydrothermal metal fluxes in convergent and collided margins. Ore Geol. Rev. 40 (1), 1–26.

Richards, J.P., 2015. The oxidation state, and sulfur and Cu contents of arc magmas: implications for metallogeny. Lithos 233, 27–45.

Roedder, E., 1971. Fluid inclusion studies on the porphyry-type ore deposits at Bingham, Utah, Butte, Montana, and Climax, Colorado. Econ. Geol. 66, 98–118.

Rowins, S.M., 2000. Reduced porphyry copper gold deposits: a new variation on an old theme. Geology 28, 491–494.

Rowins, S.M., 1999. Reduced porphyry copper-gold deposits: a newly recognized style of gold mineralization. Geological Society of Australia Abstracts 31, A–92.

Rust, A.C., Cashman, K.V., Wallace, P.J., 2004. Magma degassing buffered by vapor flow through brecciated conduit margins. Geology 32, 349–352.

Schoell, M., 1988. Multiple origins of methane in the Earth. Chem. Geol. 71, 1–10.

Shen, P., Pan, H.D., 2015. Methane origin and oxygen-fugacity evolution of the Baogutu reduced porphyry Cu deposit in the West Junggar terrain, China. Miner. Deposita 50, 967–986.

Sillitoe, R.H., 2010. Porphyry copper systems. Econ. Geol. 105, 3–41.

Simon, A.C., Frank, M.R., Pettke, T., Candela, P.A., Piccoli, P.M., Heinrich, C.A., 2005. Gold partitioning in melt-vapor-brine systems. Geochim. Cosmochim. Acta 69 (13),

3321–3335.

Smith, C.M., Canil, D., Rowins, S.M., Friedman, R., 2012. Reduced graniticmagmas in an arc setting: the Catface porphyry Cu-Mo deposit of the Paleogene Cascade Arc. Lithos 154, 361–373.

Stefanova, E., Driesner, T., Zajacz, Z., Heinrich, C.A., Petrov, P., Vasilev, Z., 2014. Melt and Fluid Inclusions in Hydrothermal Veins: the magmatic to hydrothermal evolution of the elatsite porphyry Cu-Au deposit, Bulgaria. Econ. Geol. 109, 1359–1381.

Stuart, F.M., Turner, G., Duckworth, R.C., Fallick, A.E., 1994. Helium isotopes as tracers of trapped hydrothermal fluids in ocean-floor sulfides. Geology 22, 823–826.

Sugisaki, R., Mimura, K., 1994. Mantle hydrocarbons: abiotic or biotic? Geochim. Cosmochim. Acta 58, 2527–2542.

Tafti, R., Mortensen, J.K., Lang, J.R., Rebagliati, M., Oliver, J.L., 2009. Jurassic U-Pb and Re–Os ages for the newly discovered Xietongmen Cu–Au porphyry district, Tibet, PRC: implications for metalogenic epochs in the southern Gangdese belt. Econ. Geol. 104, 127–136.

Tafti, R., Lang, J.R., Mortensen, J.K., Oliver, J.L., Rebagliati, C.M., 2014. Geology and geochronology of the xietongmen (Xiongcun) Cu-Au porphyry District, Southern Tibet, China. Econ. Geol. 109, 1967–2001.

Takagi, T., Tsukimura, K., 1997. Genesis of oxidized- and reduced-type granites. Econ. Geol. 92, 81–86.

Tang, J.X., Lang, X.H., Xie, F.W., Gao, Y.M., Li, Z.J., Huang, Y., Ding, F., Yang, H.H., Zhang, L., Wang, Q., Zhou, Y., 2015. Geological characteristics and genesis of the Jurassic No. I porphyry Cu–Au deposit in the Xiongcun district, Gangdese porphyry copper belt, Tibet. Ore Geol. Rev. 70, 438–456.

Tang, J.X., Ding, S., Meng, Z., Hu, G.Y., Gao, Y.M., Xie, F.W., Li, Z., Yuan, M., Yang, Z.Y., Chen, G.R., Li, Y.H., Yang, H.Y., Fu, Y.G., 2016. The first discovery of the low sulfidation epithermal deposit in Linzizong volcanics, Tibet: a case study of the Sinongduo Ag polymetallic deposit. Acta Geosci. Sin. 37, 461–470 (in Chinese with English abstract).

Tang, J.X., Li, Z.J., Lang, X.H., 2012. Minerals Exploration Report in the Xiongcun District, Xietongmen County, Tibet. Private Report to Tibet Tianyuan Minerals Exploration LTD (in Chinese).

Taran, Y.A., Bernard, A., Gavilanes, J.C., Lunezheva, E., CortéSc, A., Armienta, M.A., 2001. Chemistry and mineralogy of high-temperature gas discharges from Colima Volcano, Mexico: implications for magmatic gas atmosphere interaction. J. Volcanol. Geoth. Res. 108, 245–264.

Taran, Y.A., Fischer, T.P., Cienfuegos, E., Morales, P., 2002b. Geochemistry of hydro- thermal fluids from an intraplate ocean island: Everman Volcano, Socorro Island, Mexico. Chem. Geol. 188, 51–63.

Taran, Y., Inguaggiato, S., Varley, N., Capasso, G., Favara, R., 2002a. Helium and carbon isotopes in thermal waters of the Jalisco block, Mexico. Geofísica Internacional 41, 459–466.

Tarantola, A., Mullis, J., Vennemann, T., Dubessy, J., Capitani, C.D., 2007. Oxidation of methane at the $CH_4/H_2O–(CO_2)$ transition zone in the external part of the Central Alps, Switzerland: evidences from stable isotope investigations. Chem. Geol. 237, 329–357.

Tarantola, A., Mullis, J., Guillaume, D., Dubessy, J., de Capitani, C., Abdelmoula, M., 2009. Oxidation of CH_4 to CO_2 and H_2O by chloritization of detrital biotite at $270 ± 5°C$ in the external part of the Central Alps, Switzerland. Lithos 112, 497–510.

Taylor, H.P., 1974. The application of oxygen and hydrogen isotope studies to problems of hydrothermal alteration and ore deposition. Econ. Geol. 69, 843–883.

Trail, D., BruceWatson, E., Tailby, N.D., 2012. Ce and Eu anomalies in zircon as proxies for the oxidation state of magmas. Geochim. Cosmochim. Acta 97, 70–87.

Turner, G., Burnard, P.G., Ford, J.L., Gilmour, J.D., Lyon, I.C., Stuart, F.M., 1993. Tracing fluid sources and interaction. Philos. Trans. R. Soc. 344, 127–140.

Ueno, Y., Yamada, K., Yoshida, N., Maruyama, S., Isozaki, Y., 2006. Evidence from fluid inclusions for microbial methanogenesis in the early Archaean era. Nature 440, 516–519.

Ulrich, T., 2002. Geology and Alteration Geochemistry of the Porphyry Cu-Au Deposit at Bajo de la Alumbrera, Argentina. Econ. Geol. 97 (8), 1865–1888.

Vasyukova, O.V., Kamenetsky, V.S., Goemann, K., Davidson, P., 2013. Diversity of pri- mary CL textures in quartz from porphyry environments: implication for origin of quartz eyes. Contrib. Miner. Petrol. 166 (4), 1253–1268.

Wahlen, M., Tanaka, N., Henry, R., Yoshimari, T., Fairbanks, R.G., Sheruesh, A., Broecker, W.S., 1987. ^{13}C, D, and ^{14}C in methane. Eos Trans. Am. Geophys. Union 68, 1220.

Wang, C., Ding, L., Zhang, L.Y., Kapp, P., Pullen, A., Yue, Y.H., 2016. Petrogenesis of Middle-Late Triassic volcanic rocks from the Gangdese belt, southern Lhasa terrane: implications for early subduction of Neo-Tethyan oceanic lithosphere. Lithos 262, 320–333.

Wang, R., Richards, J.P., Zhou, L.M., Hou, Z.Q., Stern, R.A., Creaser, R.A., Zhu, J.J., 2015. The role of Indian and Tibetan lithosphere in spatial distribution of Cenozoic magmatism and porphyry Cu-Mo deposits in the Gangdese belt, southern Tibet. Earth Sci. Rev. 150, 68–94.

Wang, R., Tafti, R., Hou, Z.Q., Shen, Z.C., Guo, N., Evans, N.J., Jeon, H., Li, Q.Y., Li, W.K., 2017. Across–arc geochemical variation in the Jurassic magmatic zone, southern Tibet: implication for continental arc–related porphyry Cu-Au mineralization. Chem. Geol. 451, 116–134.

Watson, E.B., Wark, D.A., Thomas, J.B., 2006. Crystallization thermometers for zircon and rutile. Contrib. Miner. Petrol. 151, 413–433.

Wei, Y.Q., Zhao, Z.D., Niu, Y.L., Zhu, D.C., Liu, D., Wang, Q., Hou, Z.Q., Mo, X.X., Wei, J.C., 2017. Geochronology and geochemistry of the Early Jurassic Yeba Formation volcanic rocks in southern Tiebet: initiation of back-arc rifting and crustal accretion in the southern Lhasa Terrane. Lithos 278–281, 477–490.

Welhan, J.A., 1988. Origins of methane in hydrothermal systems. Chem. Geol. 71, 183–198.

Whiticar, M.J., 1999. Carbon and hydrogen isotope systematics of bacterial formation and oxidation of methane. Chem. Geol. 161, 291–314.

Winckler, G., Aeschbach-Hertig, W., Kipfer, R., Botz, R., Rubel, A.P., Bayer, R., Stoffers, P., 2001. Constraints on origin and evolution of Red Sea brines from helium and argon isotopes. Earth Planet. Sci. Lett. 184, 671–683.

Xiao, B., Qin, K.Z., Li, G.M., Li, J.X., Xia, D.X., Chen, L., Zhao, J.X., 2012. Highly oxidized magma and fluid evolution of Miocene Qulong Giant Porphyry Cu–Mo Deposit, Southern Tibet, China. Resour. Geol. 62, 4–18.

Xie, F.W., Tang, J.X., Chen, Y.C., Lang, X.H., 2018. Apatite and zircon geochemistry of Jurassic porphyries in the Xiongcun district, southern Gangdese porphyry copper belt: implications for petrogenesis and mineralization. Ore Geol. Rev. 96, 98–114.

Xie, Y.L., Yi, L.S., Xu, J.H., Li, G.M., Yang, Z.M., Yin, S.P., 2006. Characteristics of ore- forming fluids and their evolution for Chongjiang copper deposit in Gangdise por- phyry copper belt, Tibet: evidence from fluid inclusions. Acta Petrol. Sin. 22, 1023–1030 (in Chinese with English abstract).

Xu, W.Y., Pan, F.C., Qu, X.M., Hou, Z.Q., Yang, Z.S., Chen, W.S., Yang, D., Cui, Y.H., 2009. Xiongcun, Tibet: a telescoped system of veinlet-disseminated Cu (Au) mineralization and late vein-style Au (Ag)-polymetallic mineralization in a continental collision zone. Ore Geol. Rev. 36, 174–193.

Yang, Z.M., Hou, Z.Q., White, N.C., Chang, Z.S., Li, Z.Q., Song, Y.C., 2009. Geology of the post-collisional porphyry copper–molybdenum deposit at Qulong, Tibet. Ore Geol. Rev. 36, 133–159.

Yin, A., Harrison, M., 2000. Geologic evolution of the Himalayan-Tibetan orogen. Annu. Rev. Earth Planet. Sci. 28, 211–280.

Zajacz, Z., Seo, Z.H., Candela, P.A., Piccoli, P.M., Heinrich, C.A., Guillong, M., 2010. Alkali metals control the release of gold from volatile-rich magmas. Earth Planet. Sci. Lett. 297, 50–56.

Zhang, G.Y., Zheng, Y.Y., Gong, F.Z., Gao, S.B., Qu, W.J., Pang, Y.C., Shi, Y.R., Yin, S.Y., 2008. Geochronologic constraints on magmatic intrusions and mineralization of the Jiru porphyry copper deposit, Tibet, associated with continent-continent collisional process. Acta Petrol. Sin. 24, 473–479 (in Chinese with English abstract).

Zhao, J.X., Qin, K.Z., Li, G.M., Li, J.X., Xiao, B., Chen, L., Yang, Y.H., Li, C., Liu, Y.S., 2014. The collision-related genesis of the Sharang porphyry molybdenum deposit, Tibet: evidence from zircon U-Pb ages, Re-Os ages and Lu-Hf isotopes. Ore Geol. Rev. 56, 312–326.

Zheng, S.H., Zhang, Z.F., Ni, B.L., Hou, F.G., Shen, M.Z., 1982. Hydrogen and oxygen isotopic studies of thermal waters in Xizang. Acta Sci. Natur. Univ. Pekin 6, 99–106 (in Chinese with English abstract).

Zheng, S.H., Hou, F.G., Ni, B.L., 1983. Hydrogen and oxygen stable isotopic studies of meteoric waters in China. Chin. Sci. Bull. 13, 801–806 (in Chinese).

Zheng, Y.Y., Sun, X., Gao, S.B., 2014. Porphyry mineralization in the Gangdese Orogenic Belt. Acta Geol. Sin. (English Edition) 88, 662–664.

Zheng, W.B., Tang, J.X., Zhong, K.H., Ying, L.J., Leng, Q.F., Ding, S., Lin, B., 2016. Geology of the Jiama porphyry copper-polymetallic system, Lhasa region, China. Ore Geol. Rev. 74, 151–169.

Zheng, Y.Y., Zhang, G.Y., Xu, R.K., Gao, S.B., Pang, Y.C., Cao, L., Du, A.D., Shi, Y.R., 2007. Geochronological constraints on magmatic intrusions and mineralization of the Zhunuo porphyry copper deposit in Gangdese, Tibet. Chin. Sci. Bull. 52, 3139–3147.

Zhou, A., Dai, J.G., Li, Y.L., Li, H.A., Tang, J.X., Wang, C.S., 2019. Differential exhuma- tion histories between Qulong and Xiongcun porphyry copper deposits in the Gangdese copper metallogenic Belt: insights from low temperature thermo- chronology. Ore Geol. Rev. 107, 801–819.

Zhu, D.C., Zhao, Z.D., Niu, Y.L., Mo, X.X., Chung, S.L., Hou, Z.Q., Wang, L.Q., Wu, F.Y., 2011. The Lhasa Terrane: record of a microcontinent and its histories of drift and growth. Earth Planet. Sci. Lett. 301, 241–255.

Zhu, D.C., Zhao, Z.D., Niu, Y.L., Dilek, Y., Hou, Z.Q., Mo, X.X., 2013. The origin and pre- Cenozoic evolution of the Tibetan Plateau. Gondwana Res. 23, 1429–1454.